

i-PI 3.0: a flexible, efficient framework for advanced atomistic simulations

Yair Litman,¹ Venkat Kapil,^{1,2,3,4} Yotam M. Y. Feldman,⁵ Davide Tisi,⁶ Tomislav Begušić,⁷ Karen Fidanyan,⁸ Guillaume Fraux,⁶ Jacob Higer,⁹ Matthias Kellner,⁶ Tao E. Li,¹⁰ Eszter S. Pócs,⁸ Elia Stocco,⁸ George Trenins,⁸ Barak Hirshberg,⁵ Mariana Rossi,⁸ and Michele Ceriotti⁶

¹*Yusuf Hamied Department of Chemistry, University of Cambridge, Lensfield Road, Cambridge, CB2 1EW, UK*

²*Department of Physics and Astronomy, University College London, London, UK*

³*Thomas Young Centre, London, UK*

⁴*London Centre for Nanotechnology, London, UK*

⁵*School of Chemistry, Tel Aviv University, Tel Aviv 6997801, Israel.*

⁶*Laboratory of Computational Science and Modeling, Institut des Matériaux, École Polytechnique Fédérale de Lausanne, 1015 Lausanne, Switzerland*

⁷*Division of Chemistry and Chemical Engineering,*

California Institute of Technology, Pasadena, California 91125, USA

⁸*MPI for the structure and Dynamics of Matter, Hamburg, Germany*

⁹*School of Physics, Tel Aviv University, Tel Aviv 6997801, Israel.*

¹⁰*Department of Physics and Astronomy, University of Delaware, Newark, Delaware 19716, USA*

(Dated: May 27, 2024)

Atomic-scale simulations have progressed tremendously over the past decade, largely due to the availability of interatomic potentials based on machine-learning algorithms. These potentials enable the combination of the accuracy of electronic structure calculations with extensive length and time scales. In this paper, we present a new release of the i-PI code that allows the community to fully benefit from the rapid developments in the field. i-PI is a Python software that facilitates the integration of different methods and different software tools by using a socket interface for inter-process communication. The current framework is flexible enough to support rapid prototyping and the combination of various simulation techniques, while maintaining a speed that prevents it from becoming the bottleneck in most workflows. We discuss the implementation of several new features, including an efficient algorithm to model bosonic and fermionic exchange, a framework for uncertainty quantification to be used in conjunction with machine-learning potentials, a communication infrastructure that allows deeper integration with electronic-driven simulations, and an approach to simulate coupled photon-nuclear dynamics in optical or plasmonic cavities. For this release, we also improved some computational bottlenecks of the implementation, reducing the overhead associated with using i-PI over a native implementation of molecular dynamics techniques. We show numerical benchmarks using widely adopted machine learning potentials, such as Behler-Parinello, DeepMD and MACE neural networks, and demonstrate that such overhead is negligible for systems containing between 100 and 12000 atoms.

I. INTRODUCTION

The atomic-scale modelling of molecules and materials is a constantly evolving field driven by the interest of researchers in discovering new fundamental phenomena, interpreting complex experimental results, and, together with an increasing number of commercial enterprises, improving, discovering, and developing new materials.^[1–6] Several computational developments in recent years facilitated an extraordinary advancement of the problems that can be addressed by atomistic simulations, far exceeding the steady improvement of the underlying hardware. Arguably, the largest contribution to such fast progress can be attributed to the emergence of machine-learning interatomic potentials (MLIPs). MLIPs have cut down the computational cost of calculations with *ab initio* accuracy and allowed access to system sizes and time scales which were previously only accessible to empirical interatomic potentials.^[7–10] This has driven a renewed interest in complex simulation algorithms that were thought inapplicable for systems that require an *ab initio* quality description of their interatomic inter-

actions, such as the study of catalytic reactions ^[11–13] or thermodynamic stability of materials.^[14–16] However, the lack of easy-to-use implementations of such approaches has become an important factor that hinders their adoption by many researchers’ workflows.

Since its first release almost 10 years ago, one of i-PI’s primary objectives has been “lowering the implementation barrier to bring state-of-the-art sampling and atomistic modelling techniques to *ab initio* and empirical potentials programs”.^[17] The first iteration of i-PI was tailored to perform path integral molecular dynamics (PIMD) simulations, hence the code name. Since then, and thanks to a community effort, it has evolved into a “universal force engine for advanced molecular simulations” including standard and advanced simulations algorithms, as described in the following sections.^[18]

In the last few years, our efforts have adapted to the changing needs of the community. While continuing with the implementation of new and advanced features, we have improved the scalability of the code backend, as required by newly available and computationally efficient MLIPs. We also adopted automatic testing workflows

to strengthen the code stability and enhance our reproducibility standards.

i-PI’s capabilities as a versatile tool for atomistic simulations can be demonstrated by the wide range of applications in which it has been employed. These examples range from the dynamics of charge density wave materials[19] and nuclear motion associated to electronic excitations [20], to the elucidation of the thermodynamic properties of aqueous electrons,[21] the calculation of first principles phase diagrams,[22, 23] and the study of aqueous solutions and interfaces.[24–27] Moreover, by virtue of its modular structure, i-PI can be used as a testbed to combine different simulation “modes” to design specialized protocols tailored to the user’s requirements. We are convinced that i-PI has the potential to empower many more researchers in chemistry, physics and materials science to adopt cutting-edge simulation techniques in their research.

This manuscript reports on the progress made in the last 5 years since the release of version 2.0, by describing the newly adopted maintenance strategies, the improved performance, and the newly implemented features. The manuscript is organised as follows: In Sec. II we start with a short review of the code architecture followed by a description of the improvements made to the code’s robustness and usability and a list of main features available in this release. In Sec. III, we present a detailed discussion of the code efficiency for production and large-scale simulations, while in Sec. IV, we describe the new features since the last code release along with some numerical examples. In Sec. V, we showcase how the modularity and flexibility of i-PI help the implementation of advanced simulation setups that would otherwise require new codes to be written and Sec. VI concludes the article.

II. PROGRAM OVERVIEW

i-PI is a force engine that operates with a client-server paradigm. i-PI acts as a server in command of the evolution of the nuclear positions, while one or more instances of the client code handle the evaluation of system-specific properties. Designed to be universal, i-PI’s architecture is agnostic to the identity of the force providers, with a general and flexible backend that accommodates to a wide range of client codes.

The code is written in Python 3, a high-level, general-purpose interpreted programming language known for its emphasis on code readability. This choice facilitates rapid prototyping of new ideas and relatively easy code maintenance when compared to compiled languages traditionally used in scientific computing. Additionally, the availability of highly optimised numerical libraries allows Python-based software to deliver competitive performance. Indeed, even computing-intensive electronic structure codes have released Python implementations in recent years.[28, 29] A detailed discussion of the code

efficiency, and improvements since the previous release, is presented in Sec. III.

The communication between i-PI and the client codes is carried out through sockets, enabling local connections by shared-memory inter-process communication (UNIX domain sockets) or between two hosts connected to a local network or the Internet (TCP/IP sockets). During the initialization, i-PI creates the sockets and awaits the connection of one or more clients. When the connection is established, the simulation loop starts: i) i-PI communicates the nuclear positions and the cell lattice vector to the active clients, ii) the clients evaluate the required properties by the chosen simulation algorithm, such as energy, forces, stresses, etc, and send these back, and iii) i-PI uses this data to displace the atoms and to calculate the new nuclear positions, restarting the loop. As i-PI is designed to be client-agnostic, clients must be initialized independently before they can connect to the sockets. Importantly, the identity and number of the atoms remain constant throughout the simulations, so the geometries used to initialize i-PI and the client code must be consistent.

A schematic representation of the code structure and the server-client communication is presented in Fig. 1. i-PI is structured in a modular way that represents the underlying physics of the target simulation as faithfully as possible. To achieve this, the code is organized around the *System* class which encodes all the information related to the physical system, such as the number and identity of atoms, the ensemble to be sampled, the number of replicas in path integral simulations, the initialization procedure, and the algorithm for evolving the nuclear positions. Forces are managed through the *Forces* class, which integrates the individual force components, each of which is computed following the strategy specified in a *Forcefield* class. This two-layer approach is particularly advantageous for algorithms where the total forces and energies are obtained by a combination of these quantities computed at different accuracy levels,[30–34] or among different system portions.[35] Simulation techniques that require the evolution of many systems simultaneously make use of the *SMotion* (Systems Motion) class. This class enables the definition of evolution steps that combine the (possibly many) different systems, facilitating, for example, exchanges between system replicas as done in replica exchange simulations. Finally, estimators can be defined within the code or computed by the provided post-processing tools or user-generated scripts.

For the sake of completeness, we report an updated list of the code features in section IID.

A. Why you might want to get involved: a developer perspective

There are numerous reasons for contributing to i-PI that developers in the field might find compelling. We summarise some of the key arguments below.

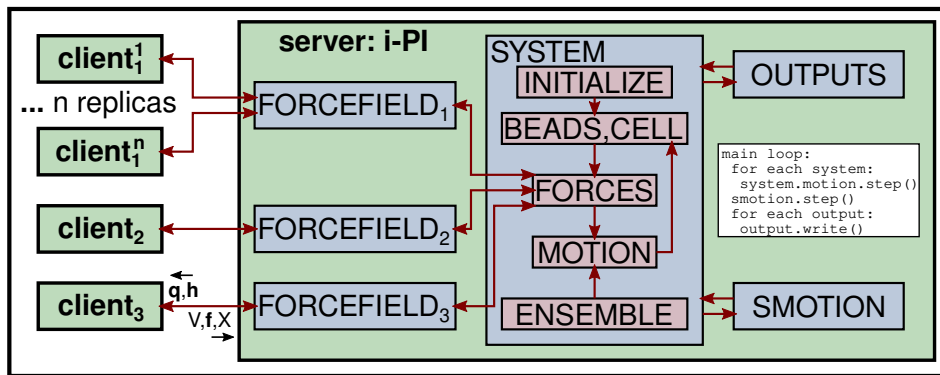


FIG. 1. Schematic representation of the i-PI code structure and the server-client communication. The physical system is defined by one or more replicas (beads), and the sampling conditions (e.g. temperature and pressure) by an *Ensemble* class. The forces acting on the atoms are constructed based on a combination of energy contributions evaluated by one or more instances of the *Forcefield* class (three in this example). Each *Forcefield* instance communicates with a different client sending positions (\mathbf{q}) and lattice vectors (\mathbf{h}), and receiving energy (V), forces (\mathbf{f}), stresses and possible extra properties (X) as a JSON formatted string. In simulations with multiple replicas, each *Forcefield* instance can accept connections from several clients, to achieve parallel evaluation. The *Motion* class determines the evolution of the atoms (e.g. time integration, or geometry optimization), while “system motion” classes (*SMotion*) can act on multiple systems, e.g. to carry out replica exchange simulations. The output class handles writing the output and restart files.

Many available clients codes: i-PI is connected to a multitude of electronic-structure and machine learning codes, either directly or through its ASE [36] or LAMMPS [37] interfaces. This wide-ranging connectivity means that a single implementation is readily available to all the users of these codes, which significantly amplifies the potential impact of each contribution to i-PI.

Lower development and maintenance effort: Similarly, in scenarios where a developer aims to use a newly implemented algorithm with different types of codes, such as a density functional theory (DFT) plane wave code to study periodic systems, or a quantum chemistry code to study gas phase molecules at a higher electronic structure level, two separate implementations would be required. By integrating the algorithm into i-PI, only one implementation is required and there is only one code to maintain.

Automatic (re)evaluation of physical quantities: i-PI’s infrastructure automatically manages updates of energy, forces, stresses, and other structure-dependent properties by establishing dependencies between physically related variables. This enables developers to concentrate solely on the algorithm’s implementation making the development process more focused and efficient.

B. Code robustness and usability

The significant increase of i-PI users and contributions over the last years, primarily from scientists outside the core developers’ research groups, required enhancing the maintainability, robustness, and standardization of the code. These improvements involve five distinct aspects:

Documentation: The documentation of the i-PI code is now generated with *Sphinx* and available online.

It is easily accessible at <https://ipi-code.org/i-pi/index.html> and linked to the main code webpage. The documentation has been updated to reflect the current status of the code, and a section about how to contribute new features to the code has been added to reduce the barrier for new developers. An automatic parsing of the doc strings throughout i-PI ensures a complete listing of all possible keywords and the corresponding explanation, which is automatically updated as soon as new features are implemented and merged in the main branch.

Examples: We have completely restructured the provided examples to make them as intuitive as possible for newcomers. The examples are now organized into three folders, namely *features*, *clients*, and *hpc-script*. The *features* folder displays extensive examples of the different implemented functionalities, all of which can be run locally using the built-in Python or Fortran driver, without requiring additional software installation. The *clients* folder includes examples tailored to specific driver codes, highlighting the unique syntax and tags needed for an adequate setup when used in connection to i-PI. At the moment, we provide examples for ASE,[36] CASTEP,[38] CP2K,[39] LAMMPS,[37] DFTB+,[40] ffsGDML,[41] FHI-aims,[42] librascal,[43] Quantum Espresso,[44–46] VASP,[47] elphmod,[48] and YAFF.[49] We note, however, that many other codes can also be connected to i-PI through their ASE and LAMMPS interfaces. Finally, motivated by the number of user queries on this topic, the *hpc-scripts* folder provides examples with the corresponding submission scripts to run the simulations on high-performance computing platforms.

Demonstrations and tutorials: We have added more complex examples to illustrate the application of i-PI in realistic simulation scenarios, combining several of the

features showcased in the *examples* folder. Some of these demonstration examples also cover some of the use of the pre- and post-processing scripts accompanying the code. Users specifically interested in learning the theory of path integral simulations and obtaining hands-on practice using i-PI are referred to the online courses developed with this goal <https://tinyurl.com/pimd-mooc> or <https://github.com/i-pi/piqm2023-tutorial/>.

Continuous integration: We have implemented continuous integration workflows to automatically test for the code’s functionality. One of the automatic workflows reviews all the simulations in the *examples* folder by running them for a few steps and quickly verifying if they are functioning correctly. A second workflow performs regression tests. In these cases, the simulations are performed for the required amount of steps and the simulation outputs are compared against pre-computed reference values. Together, these workflows guarantee that any new modification to the code neither alters the results of simulations nor breaks the provided examples. Additional workflows, less critical for the functioning of the code, focus on checking the formatting syntax using flake8 (<https://flake8.pycqa.org/>) and black (<https://github.com/psf/black>), or managing the updates of PyPI releases.

Modifications and additions to i-PI: To add or modify the source code, contributors must create a pull request in the GitHub repository of i-PI <https://github.com/i-pi/i-pi>. The contributors must ensure that all the automatic tests pass successfully. When introducing a new feature, contributors are expected to provide a minimal example that runs with built-in drivers, along with the corresponding regression test to guarantee the long-term stability of the new feature. After these criteria are met, the actual code review starts. During the review process, the code managers might ask the contributor to justify some design decisions, modify part of the code contribution, improve the documentation, etc. Finally, when all the requested changes are fulfilled, the new addition is merged into the main branch of the code.

C. How to implement an i-PI interface in my code?

For softwares that provide a Python interface to directly compute energy and forces for a given structure, such as several machine-learning potentials, it is often possible to create an interface with a few dozen lines of code using the provided Python driver, available in the `drivers/py/` folder. In the rest of the cases, the simplest method to implement the communication interface is to identify in the target client software an existing loop that updates nuclear positions as it is done in any geometry optimization or molecular dynamics algorithm. The beginning and the end of this loop are the places where the client code will receive the atomic coordinates from i-PI and send back energy, forces, stress tensor and other

requested quantities (see section IV B), respectively. In several scenarios, such as the one dealing with electronic structure codes or some MLIPs, the client code would have to carry out the appropriate initialization routines before the client establishes a connection with the i-PI server. Given that such initialization requires knowledge of the types of atoms (that are not communicated by i-PI), it is often necessary to provide a separate description of the structure in the format expected by the client code. Most of the electronic structure clients offer the possibility of using the converged density matrix/wavefunction from a previous step as the initial guess for the subsequent calculation. Consequently, the self-consistent cycle converges as quickly using i-PI as it would with the same algorithm implemented within the client code. Examples of interface implementations in Python and Fortran can be found in the *driver* folder provided with the code, while a C++ implementation can be found in the LAMMPS code.[37]

D. Main Features

We conclude this section by listing the main features available in the 3.0 release:

Classical and path integral molecular dynamics: in the *NVE*, *NVT*, *NPT* and constant stress (N_sT) ensembles.

Thermostats: stochastic velocity rescaling,[50] path-integral Langevin equation thermostats,[51] generalized Langevin equation (GLE) thermostats, including the optimal sampling,[52, 53] quantum, [54], δ ,[55] hot-spot, [56] and PIGLET thermostats,[57] dynamical corrections to Langevin trajectories,[58] fast forward Langevin thermostat,[59] Langevin sampling for noisy and/or dissipative forces.[60, 61]

Barostats: isotropic barostats,[17, 62] anisotropic barostats,[63] and its path integral adaptations.[64, 65]

Geometry optimizers: steepest descent, L-BFGS, trust radius BFGS, etc, nudged elastic band [27, 66, 67] and mode following saddle point search.[68]

Vibrational analysis: through the harmonic Hessian, independent mode framework, the vibrational self-consistent field, and self-consistent phonons.[69]

Enhanced sampling and free energy calculations: thermodynamic integration,[70], metadynamics, replica exchange MD,[71] and quantum alchemical transformations.[72, 73]

Multiple time-stepping (MTS): MTS in real time and imaginary time, also known as ring polymer contraction.[30, 31, 34, 35]

Approximate quantum dynamics calculations: ring polymer molecular dynamics (RPMD),[74, 75] centroid molecular dynamics (CMD),[76, 77] thermostatted RPMD,[58, 78] path integral coarse graining,[79] ring polymer instanton rates and tunnelling splittings.[80]

Advanced path integral simulations and estimators: fourth-order path integrals,[81] perturbed path

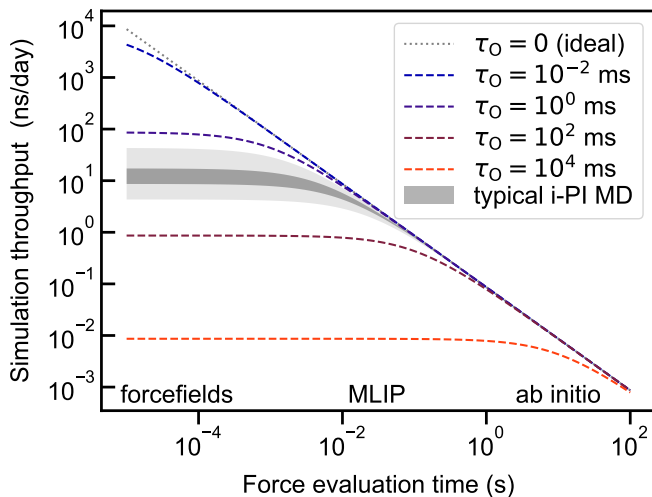


FIG. 2. Simplified picture of the impact of a given overhead τ_O on the simulation throughput (expressed in ns/day, assuming a time step of 1 fs) as a function of the force evaluation cost. An overhead of about 10 ms (typical for a moderately complicated simulation with i-PI 2.6) is negligible when used with *ab initio* force evaluations, but becomes significant for the most efficient (or heavily-parallelized) machine-learning potentials.

integrals,[82] open path integrals,[83] the scaled-coordinate heat capacity estimator,[84] isotope fractionation estimations,[85] particle momentum distribution,[86] reweighted fourth-order path integral MD.[87, 88]

Path Integral Molecular Dynamics (PIMD) for indistinguishable particles: Methods for simulating bosons,[89] with improved quadratic scaling,[90] and fermions, through a reweighting procedure.[91]

Cavity MD (CavMD): Simulation of systems confined in optical or plasmonic cavities.[92, 93]

Non-linear spectroscopy: Evaluation of non-linear spectroscopic observables by equilibrium non-equilibrium simulations for classical and quantum nuclei.[94–96]

Molecular dynamics driven by Electronic Structure Quantities: non-adiabatic tunnelling rates in metallic systems,[97, 98] molecular dynamics with with time-dependent external fields.

Committee MLIP: committee models, baseline energy model and uncertainty estimation.[99, 100]

III. EFFICIENCY OF LARGE-SCALE SIMULATIONS

i-PI’s socket-based communication and Python architecture offer convenience and flexibility to implement new and advanced simulation algorithms, facilitating integration with other codes. This flexibility, however, comes at the price of a computational overhead associated with UNIX- and TCP-socket communications, and Python’s inherent inefficiency compared to lower-level languages such as Fortran, C, and C++. To analyse i-PI’s overhead

on the performance of the simulations, it is instructive to separate the intrinsic wall-clock time needed to evaluate energy and forces, τ_F , and i-PI’s overhead, τ_O , such that the length of simulation that can be obtained for a certain computational effort is proportional to $1/(\tau_F + \tau_O)$. The initial focus of i-PI was on *ab initio* force providers, where τ_F is of the order of seconds, and therefore an overhead of the order of $\tau_O \sim 10$ ms was inconsequential (Fig. 2). However, with MLIPs becoming the primary tool for large-scale, reactive calculations, an overhead of several ms can become the performance bottleneck. Therefore, we have reevaluated i-PI’s efficiency for this release.

We decided to benchmark i-PI against the C++ based LAMMPS code, since this choice allows us to disentangle and quantify the communication and Python’s overhead and also to analyze production simulations using popular MLIPs, that are interfaced with LAMMPS. The overall cost of an i-PI simulation can be assessed by using a dummy driver that returns zero energy and forces. The communication cost can be removed by disabling the force evaluation altogether, which can be achieved by setting `weight="0"` as an attribute of the `<force>` components. Performing these benchmarks for the simplest case of constant-energy *NVE* MD and varying the number of atoms allowed us to determine a lower bound for τ_O , and to subdivide it into the cost of the integrator and that of the communication (Fig. 3). It is clear that for this simple setup, with $\tau_F = 0$, LAMMPS is almost 10 faster than i-PI 2.6 in the limit of large simulations. The relative overhead of i-PI becomes very large for a small number of atoms, where LAMMPS performs millions of steps per second, whereas i-PI 2.6 reached a hard limit of about 1 ms/step. The cost (per MD step) of these simulations can be roughly modelled as a constant term plus a per-atom contribution so that the overhead can be estimated as $\tau_O \approx A + B N_{\text{at}}$. Note that for such a wide range of system sizes it is not advisable to determine the coefficients by linear regression, because the intercept would be affected by large relative errors, and so we determine A as the time per step of the smaller simulation (8 atoms) and B as the time per step per atom of the largest one (2^{16} atoms).

Fig. 3 also compares the stable 2.6 version with the new 3.0 release. In the latter, we performed several optimizations to reduce the overhead associated with accessing the i-PI *depend* objects,[17] substituted explicit loops with array operations, and removed other obvious bottlenecks from the implementation. This reduced the overhead of the *NVE* integrator by a factor of 3-5, and the communication overhead by a factor of 2. Table I compares the value of the A and B coefficients for different simulation setups; in all cases, the new release dramatically reduces both constants, so that for most classical MD simulations and up to a few 1000s of atoms one can now expect an overhead of a few ms per step. It is thus possible to perform tens of millions of simulation steps per day when disregarding the force evaluation costs. The over-

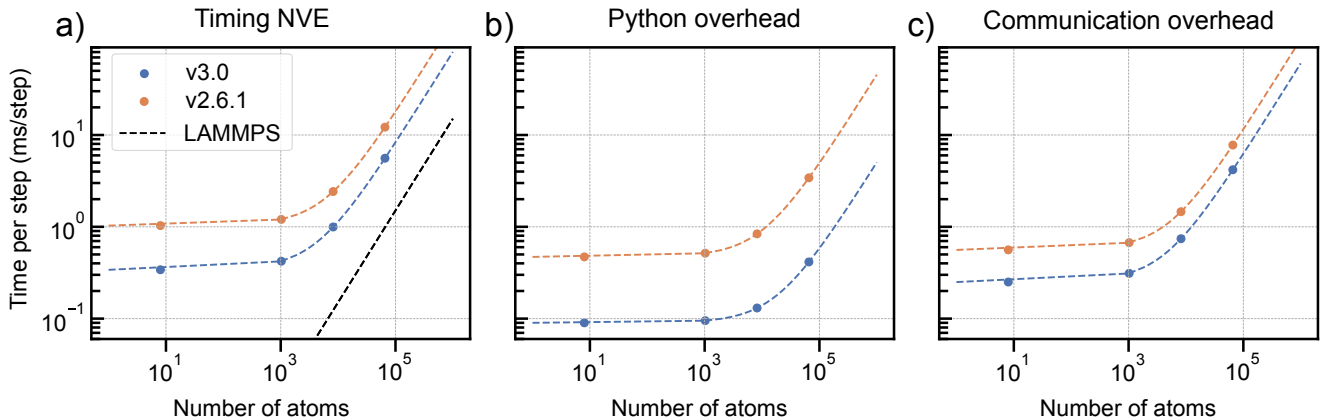


FIG. 3. (a) System size dependence of the timing per step when performing a NVE simulation of an ideal gas using LAMMPS, and when using i-PI with a dummy driver that returns zero energy and forces, communicating through UNIX sockets. The overhead relative to LAMMPS is also broken down into (b) a base Python overhead (obtained by repeating the i-PI simulation with no forcefield and subtracting the LAMMPS timings) and a remainder, that is associated with the communication overhead (c). Markers correspond to actual simulations while the dashed lines are fits to $\tau_O = A + BN_a$, where N_a is the number of atoms.

type	replicas	socket	ensemble	thermostat	A / ms		B / ($\mu\text{s}/N_a$)	
					i-PI 2.6	i-PI 3.0	i-PI 2.6	i-PI 3.0
MD	1	none	NVE	none	0.47	0.09	0.06	0.02
MD	1	UNIX	NVE	none	1.03	0.34	0.17	0.08
MD	1	TCP/IP	NVE	none	21.54	1.26	0.64	0.10
MD	1	none	NVT	svr	0.56	0.14	0.07	0.03
MD	1	none	NVT	langevin	0.86	0.22	0.24	0.21
MD	1	none	NPT	langevin	1.45	0.47	0.37	0.32
MD	1	none	NPT	svr	1.13	0.38	0.22	0.13
PIMD	2	none	NPT	pile.l	1.39	0.47	0.94	0.60
PIMD	2	UNIX	NPT	pile.l	2.62	1.27	1.32	0.76
PIMD	2	TCP/IP	NPT	pile.l	32.64	2.45	1.68	0.77
PIMD	32	none	NPT	langevin	2.73	0.67	17.21	12.97
REMD	4 × 6	none	SC-NPT	langevin	27.80	16.86	11.29	12.50

TABLE I. Comparison between the timings for the tests in the `ipi_tests/profiling` folder with i-PI versions 3.0-alpha2 or 2.6.3. The coefficients A and B can be used to estimate the overhead for a given number of atoms N_a , as $\tau_O = A + BN_a$. In the table, (PI)MD indicate simulations performed with (path integral) MD; “socket” indicates the type of communication, *none* corresponding to simulations that avoid entirely force evaluations. Thermostats are chosen between stochastic velocity rescaling, *svr*, [101] plain Langevin, and path-integral Langevin. [51] The last line corresponds to a complex setup combining path integral and replica-exchange molecular dynamics (REMD) with 4 beads and 6 ensemble replicas and a finite-difference evaluation of Suzuki-Chin (SC) high-order path integrals. [81, 102]

head is larger when considering simulations with multiple replicas, and/or complicated setups that involve e.g. high-order path integration or replica exchange. Often, however, these advanced simulation techniques allow cutting on the overall cost of a calculation by reducing the number of force evaluations to reach the desired convergence of accuracy, which is a key advantage in using i-PI over faster, but less feature-rich, alternatives. An example that is also relevant to classical MD trajectories is the presence of BAOAB integrators, [103] which allows dou-

bling the time step in simulations of liquid water. A technical detail we also want to highlight from Table I is the $> 20\times$ reduction of the constant overhead for TCP/IP communication. This is due to the disabling of Nagle’s algorithm, [104] which was found to interfere negatively with the transfer of small messages in the i-PI communication protocol. This change has to be enacted also on the client side, so we urge developers of packages that contain an i-PI interface to apply similar changes.

Even though this release cuts significantly on the

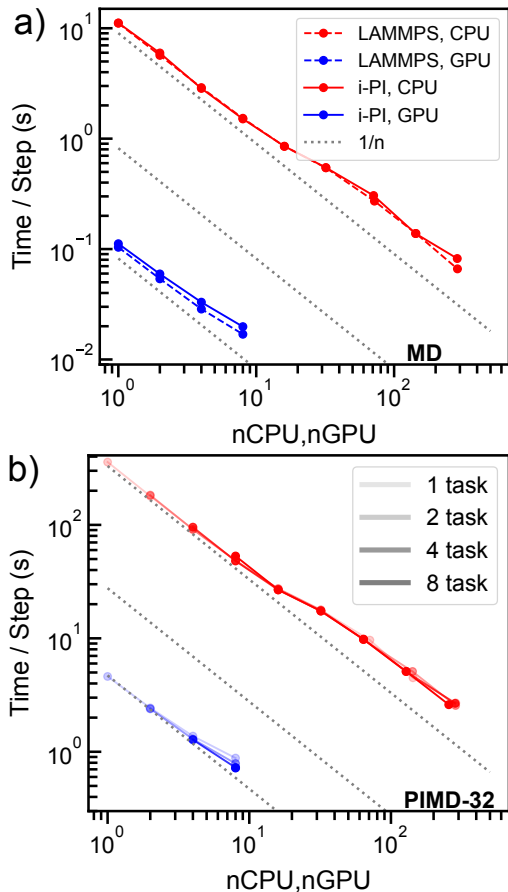


FIG. 4. Timings for 1 step of NVT dynamics with Langevin thermostating, for a box containing 4096 water molecules at ambient temperature and density, using a DeepMD model,^[105] using the LAMMPS implementation.^[106, 107] Simulations are run on nodes with 2 Intel(R) Xeon(R) Platinum 8360Y, with 36 cores each (CPU) and nodes with 2 NVIDIA V100 cards (GPU). Parallelization is based on MPI, leveraging the LAMMPS domain decomposition. (a) Timings for MD simulations. Dashed and full lines correspond to simulations performed with LAMMPS, and i-PI using LAMMPS/DeepMD as a driver, respectively. (b) Timings for PIMD simulations with 32 replicas. The shading of the curves indicates the number of independent LAMMPS tasks that are connected to i-PI, and the number of processing units indicates the sum across all tasks.

i-PI overhead, and we are committed to further reducing it in the future, it is important to determine whether and when it matters in practical use cases. To this end, we consider the task of simulating 4096 water molecules at room temperature, in the canonical *NVT* ensemble. We start by considering the LAMMPS implementation of a DeepMD neural network, that is used both to perform MD directly using its LAMMPS implementation,^[7, 106, 107] and as a driver for both classical MD and path integral molecular dynamics with i-PI. On the hardware we use for this test (Intel(R) Xeon(R) Platinum 8360Y processors with 2 GPU NVIDIA V100

cards/node), a single-point evaluation of energies and forces on one CPU requires approximately 10s, which is several orders of magnitude longer than the corresponding i-PI overhead (approximately 2 ms/step). In practical scenarios, however, the MLIP calculation will be heavily parallelized, either using a multi-CPU implementation or using one or more GPUs. As shown in Fig. 4, the i-PI overhead remains negligible up to the highest parallelization level for CPUs (up to 4 nodes, 288 cores), even though the practical overhead at the full-node level is higher than expected because of the need of dedicating one core to the execution of i-PI. The GPU implementation of DeepMD is much faster and can be parallelized efficiently up to about 8 GPUS (4 nodes), for which (with a time step of 0.5 fs) LAMMPS clocks almost 2.5 ns of simulation per day. We observed the empirical i-PI overhead with LAMMPS DeepMD to be up to 10 times larger than that seen with the dummy driver, which we could trace to unnecessary reconstructions of the neighbor list. We then optimized the LAMMPS interface of the driver, minimizing the number of neighbor list updates and reducing the overhead to be less than 20% for the highly-efficient multi-GPU setup. For a PIMD setup, i-PI allows exploiting an additional level of parallelism by running multiple drivers in parallel. Given that this is a trivial type of parallelization, it can improve the scaling whenever the client code shows less-than-ideal scaling, as is seen for the GPU implementation of DeepMD.

model	architecture	n_{PU}	n_{H_2O}	τ_F/s	throughput (ns/day)	
					direct	w/i-PI
DeepMD	CPU (Xeon)	288	4096	0.066	0.65	0.53
DeepMD	GPU (V100)	8	4096	0.017	2.54	2.16
MACE	GPU (A100)	1	4096	1.47	0.03	0.03
MACE	GPU (A100)	1	64	0.047	0.94	0.92
BPNN	CPU (Xeon)	768	4096	0.015	2.95	2.00

TABLE II. An overview of the expected throughput for *NVT* MD simulations of liquid water for different system sizes, hardware, and MLIPs. DeepMD simulations timings correspond to the highest level of parallelization in Fig. 4; MACE simulations use the ASE driver with the MACE-MP-0 model(S),^[9] single precision and were run on one A100 GPU card. We note, however, that the ASE driver is not the most efficient way of running MACE, but regardless, the overhead of i-PI is negligible compared to a MACE force evaluation. Behler-Parrinello neural network simulations use the model from Ref. ^[108], and were run using the n2p2 interface in LAMMPS, on a Intel® Xeon® E5-2690 v3 @ 2.60GHz.

A simple estimate of the throughput of an i-PI calculation.

These experiments show that, in practical use cases, the overhead introduced by i-PI is negligible or small up to high levels of parallelization of the MLIP code – al-

though one should reassess these conclusions depending on the hardware, the specific MLIP implementation, and the type of simulation performed. As shown in Fig. 2, a practical recipe to determine what throughput one can expect out of the combination of i-PI with your favourite machine-learning code is to determine the overhead τ_O , either from Table I or by running a short simulation with a dummy driver. A dummy calculation is also suitable to tune the simulation parameters (and potentially to help remove bottlenecks from other simulation pathways). The cost of evaluating energy and forces τ_F , also depends on the type of MLIP, system size and the hardware of choice. Thus, by comparing the τ_O and τ_F it is possible to determine whether the i-PI overhead is significant.

As shown in Table II, for both small and medium-sized supercells, and for DeepMD, n2p2 and MACE models, a standard constant-temperature MD simulation is limited by τ_F . The only exception is DeePMD(GPU), which as mentioned earlier, appears to be specific to this setup and due to reasons we continue to investigate. In summary, using i-PI as a driver not only does not prevent reaching a few million energy evaluations per day, corresponding to several ns for typical MD time steps, but also allows access to advanced simulation methods, such as path integral molecular dynamics, as well as facile interfacing with new MLIPs implementations.

IV. DESCRIPTION OF SELECTED FEATURES

A. Bosonic and Fermionic Path Integral Molecular Dynamics

Exchange effects, arising from bosonic and fermionic statistics, are important in simulations of phenomena such as superfluidity,[109] supersolidity,[110] and superconductivity. However, ordinary PIMD simulations assume that the atoms are distinguishable particles and obey Boltzmann statistics. The biggest challenge in going beyond this assumption and performing PIMD simulations of indistinguishable particles is including all the possible identical particle permutations in the partition function. These are taken into account by connecting rings of permuted particles to form larger polymers.[89] Since there are $N!$ permutations of N particles, the simulation, in principle, should sum over the spring forces from $N!$ configurations, which quickly becomes intractable.

The new version of i-PI supports PIMD simulations that include exchange effects, using an algorithm introduced by Hirshberg *et al.*[89, 90] In this approach, PIMD simulations of bosons scale quadratically,[90] rather than exponentially, with N . This is achieved by replacing the standard ring polymer potential with $V_B^{(N)}$, which is de-

finied by the recurrence relation,

$$e^{-\beta V_B^{(N)}} = \frac{1}{N} \sum_{k=1}^N e^{-\beta (V_B^{(N-k)} + E_N^{(k)})}. \quad (1)$$

Here, $E_N^{(k)}$ is the spring potential of a ring polymer connecting the particles $N - k + 1, \dots, N$ in a cycle, and $V_B^{(0)} = 0$. This potential, and the forces it induces, are computed in quadratic time with N and in linear time with the number of beads.[90]

The i-PI implementation allows the efficient simulation of systems composed of ~ 1000 particles. A comparison of the scalability of bosonic and standard PIMD simulations in i-PI is presented in Fig. 5, using the same normal-mode integrator (**bab**, see below) in both cases. The bosonic simulation has quadratic scaling while the distinguishable one scales linearly. For $N = 64$ particles, the cost of bosonic exchange effects is approximately 12 times that of standard PIMD, and for $N = 1024$ it is only 44 times slower with the same integrator.

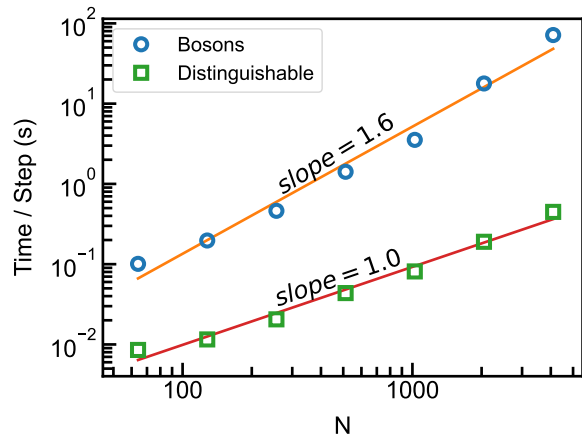


FIG. 5. Scaling with the number of particles of the propagation of the spring forces in Cartesian coordinates, for distinguishable and bosonic systems. Both simulations were run with the **bab** propagator with **nmts=10**.

Using bosonic PIMD in i-PI is straightforward, and involves adding the following section to the xml input file:

```
<normal_modes propagator='bab'>
  <bosons>...</bosons>
  <nmts>M</nmts>
</normal_modes>
```

The bosonic atoms are listed using the **bosons** tag. This can be done as a list of atoms (zero-based), such as `<bosons id='index'> [0, 1, 2] </bosons>`, or by a list of labels, such as `<bosons id='label'> ['He'] </bosons>`. At the moment, the integration should be done in Cartesian coordinates (**normal_modes propagator='bab'**), because an analytic expression for the normal-modes propagator

of the free ring polymer part of the Hamiltonian is known for bosons. Because the frequencies of the springs are typically higher than the physical frequencies, the use of multiple-time stepping in the Cartesian integrator is recommended (via the `nmts` tag, where `M` is the factor by which to reduce the timestep).

In Fig. 6, we present the average energy of 512 trapped, non-interacting cold bosons. By comparing with distinguishable particle simulations, the relevance of exchange effects becomes evident.

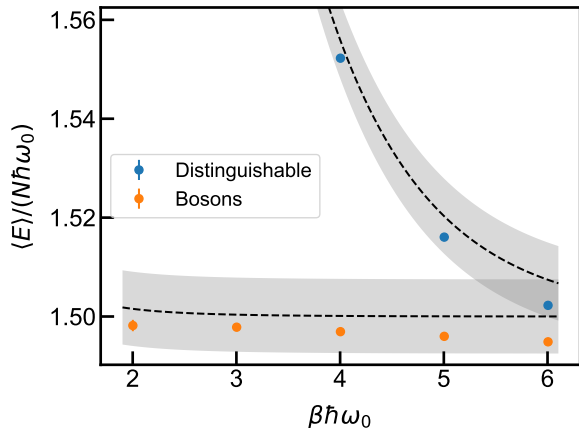


FIG. 6. The energy per particle of $N = 512$ trapped non-interacting bosons as a function of temperature (indicated by the dimensionless number $\beta\hbar\omega_0$, where ω_0 is the harmonic trap constant), with $P = 42$ beads. The shaded areas indicate an error region of $\pm 0.5\%$.

A way to assess the extent of exchange effects in bosonic simulations is to analyse the following system properties provided within i-PI: (1) `exchange_distinct_prob`, which is the probability of the ring-polymer configuration corresponding to distinguishable particles:

$$\frac{1}{N! \cdot e^{-\beta V_B^{(N)}}} e^{-\beta (\sum_{i=1}^N E_i^{(1)})}, \quad (2)$$

where $E_i^{(1)}$ is the spring potential of the ring polymer connecting the beads of particle i in a separate ring. This quantity tends to 1 in the regimes where exchange is negligible. (2) `exchange_all_prob`, which is the probability of the ring-polymer configuration connecting *all* the bosons, scaled by $1/N$:

$$\frac{1}{e^{-\beta V_B^{(N)}}} e^{-\beta \cdot E_N^{(N)}}, \quad (3)$$

where $E_N^{(N)}$ is the spring potential of the ring polymer connecting all the particles $1 \rightarrow 2 \dots \rightarrow \dots \rightarrow N \rightarrow 1$ in one large ring. This quantity is high in regimes of effective exchange between all the particles. In Fig. 7, we show the average of `exchange_all_prob` in converged simulations of trapped cold noninteracting bosons as a

function of temperature. This quantity tends to 1 in the limit $T \rightarrow 0$, $\beta \rightarrow \infty$, in which all permutations are equally probable. [89]

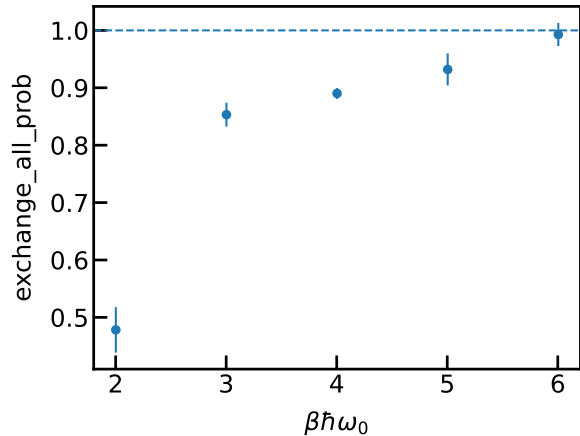


FIG. 7. The probability of the ring polymer configuration that connects all $N = 16$ non-interacting trapped particles at different temperatures (indicated by the dimensionless number $\beta\hbar\omega_0$, where ω_0 is the harmonic trap constant).

Several estimators require modification when performing bosonic PIMD simulations. For example, the primitive estimator for the kinetic energy (`kinetic_td`) is modified according to Eq. 1 (as shown in Eq. (2) in the SI of Hirshberg *et al.* [89]) while the standard virial kinetic energy estimator can be used for bosons in confined systems. On the other hand, the centroid-virial kinetic estimator is not applicable due to the lack of an appropriate centroid definition.

Lastly, fermionic statistics can be obtained by first performing bosonic simulations and then reweighting the results.[91, 111, 112] This is done by using the fermionic sign estimator (the `fermionic_sign` property of i-PI). For every position-dependent operator, the corresponding fermionic estimator is obtained from the bosonic estimator by multiplying with the fermionic sign, and dividing by the average fermionic sign in the simulation (see Eq. (9) of Ref. [91]). The average sign is always positive but for simulations at low temperatures or with large N , where the sign problem is severe, it gets close to zero. Fig. 8 illustrates the behaviour of the fermionic energy estimator for $N = 3$ non-interacting, trapped fermions at several temperatures. While the distribution of the bosonic energy estimator throughout the simulation is always positive, the fermionic energy estimator changes sign, its distribution is bi-modal around $E = 0$, and more symmetric at lower temperatures. The massive cancellations of positive and negative contributions make the mean fermionic energy harder to converge in comparison to the bosonic case.

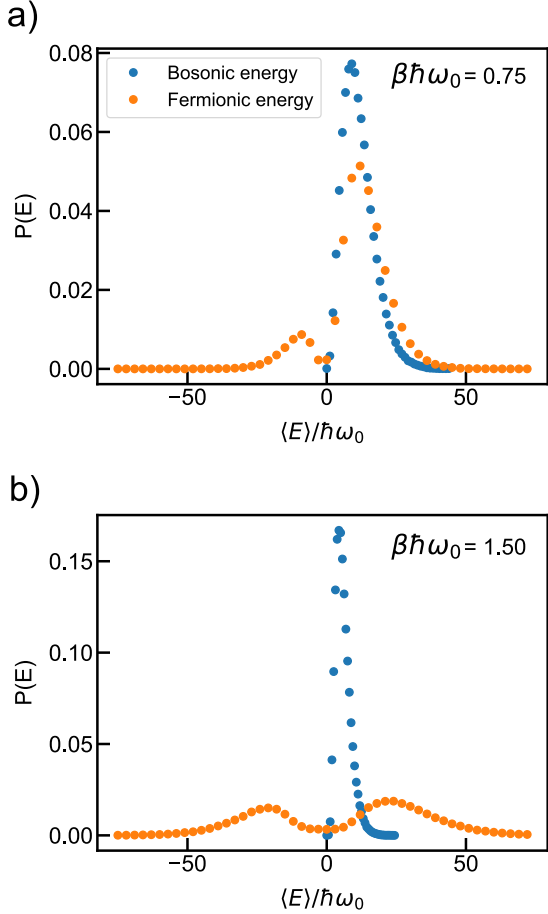


FIG. 8. The distribution of bosonic and fermionic energy estimator, $P(E)$, for $N = 3$ trapped non-interacting particles at two representative temperatures indicated by the dimensionless number $\beta\hbar\omega_0$, where ω_0 is the harmonic trap constant.

B. Nuclear propagation by additional dynamical variables

i-PI 3.0 can employ numerical quantities provided by the driver (beyond the usual forces and stress arrays) to run advanced types of dynamics. This supplementary communication is achieved through an additional string that can be passed in the `extras` field of i-PI within the same socket communication. When such string is JSON-formatted, an automatic parser makes the respective quantity available in the code and accessible as a dictionary. More importantly, when the data is numeric, it is added as a property of the force object, guaranteeing a seamless integration with other i-PI features, and becoming available to be used in any type of algorithm. In the next section, we present two examples of advanced simulations that employ electronic structure quantities as “additional” variables to modify the atomic forces and therefore alter the nuclear dynamics.

1. Non-adiabatic tunnelling rates in metallic systems

The vanishing band gap in metals allows for nuclear movements to induce electronic excitations, even at relatively low velocities. These effects are not captured by the Born-Oppenheimer approximation and therefore are collectively referred to as non-adiabatic effects (NAEs). NAEs in metals are qualitatively different from the ones found in molecules, due to the continuous manifold of available empty electronic states present in the former, and thus require a different set of theoretical approaches. A frequently used technique to simulate these types of NAEs is to decorate the otherwise Born-Oppenheimer dynamics with an electronic frictional kernel and a stochastic force.[113–115] The electronic friction formalism has been derived from first principles starting from the exact factorization of the wave function, initially at 0 K,[116, 117] and more recently at finite temperatures.[118] Moreover, in the case of a theory of non-interacting electrons, such as DFT, the friction kernel can be computed explicitly from *ab initio* calculations.[119]

When studying the kinetics of light atom diffusing in metals, NQEs can become as important as NAEs. To address this complex problem some of the authors have recently derived a theoretical framework that can capture both types of effects.[97] The method called ring polymer instanton with explicit friction (RPI-EF) was derived by combining the semiclassical instanton rate theory in its path integral discretized form,[120] with the *ab initio* electronic friction formalism. The framework is general enough to incorporate the spatial and frequency dependence of the friction tensor and, owing to the computational efficiency of the parent methods, [121, 122] it is suitable for first-principles calculations of reaction rates in complex, high-dimensional systems.[98]

The RPI-EF method is algorithmically similar to classical Eyring transition rate theory and requires the search of a first-order saddle point. In this case, however, the saddle point is not the reaction transition state but rather an imaginary time trajectory that makes the Euclidean action stationary. This special trajectory is known as instanton and can be interpreted as the main tunnelling pathway.[123] In the limiting case of a position-independent friction kernel (see a more general expression in Ref. [97]) the discretized Euclidean action, S_P can be expressed as

$$S_P = S_P^{\text{sys}} + \hbar \frac{\beta}{P} \sum_{l=-P/2+1}^{P/2} \sum_{i=1}^{3N} \frac{\tilde{\eta}(\omega_l)\omega_l}{2} (Q_i^{(l)})^2, \quad (4)$$

where P is the number of discretization points or beads, N is the number of atoms, β is the inverse temperature, $Q^{(l)}$ represents the free ring-polymer normal mode coordinates, ω_l are the free RP normal mode frequencies, and $\tilde{\eta}$ is the Laplace transform of the (electronic) friction kernel. The RPI-EF calculation consists of a series

of geometry optimizations using progressively more discretization points until the converged instanton pathway is achieved. A detailed description of the individual steps involved in RPI and RPI-EF simulations, as well as practical guidelines, can be found elsewhere.[98, 124, 125]

The i-PI implementation of RPI-EF builds upon the RPI implementation from the previous i-PI release. The primary distinction regards the additional terms that contain the friction kernel. In the case of a position-dependent friction, these terms require updates at each step of the geometry optimization, which has been made possible by the new JSON string communication described earlier. The friction terms are enabled by setting the friction flag inside the instanton block, `frictionSD`. Since the theory assumes that the frequency dependence of the friction kernel is position-independent, the user needs to provide the normalized spectral density, $\tilde{\eta}(\omega)$, that can be specified with the flag `fric_spec_dens` and the energy at which it has been normalized to one by using the flag `fric_spec_dens_ener`. A minimal example of the section `motion` to run RPI-EF simulations with i-PI is

```
<motion mode='instanton'>
  <instanton mode='rate'>
    <friction>true</friction>
    <fric_spec_dens mode='file' >
      fric_spec_dens.dat
    </fric_spec_dens>
    <fric_spec_dens_ener> 0.1
    </fric_spec_dens_ener>
    <hessian_update>powell</hessian_update>
  </instanton>
</motion>
```

In Fig. 9, we present the instanton geometry obtained for a double well potential without friction, with constant friction, and with a position-dependent friction. The inclusion of constant friction causes the particle to behave more classically, resulting in the shrinkage of the instanton geometry when compared to the calculation without friction. The position-dependent friction result shows that the instanton geometry avoids regions with large friction, indicating that non-adiabatic effects can steer the main tunnelling pathway and, consequently, steer quantum dynamics.[98]

2. Dynamics with time-dependent external field

Recent experiments have shown that the excitation of infrared-active phonons through THz laser pulses leads to a vast phenomenology in different kinds of materials.[126] These phenomena are non-thermally driven by microscopic processes rather than originating from ultrafast heating effects.[127] The possibility for driving materials, ranging from traditional solids to liquids and interfaces, across phase transitions and into metastable states that are not accessible at thermal equilibrium, has opened the

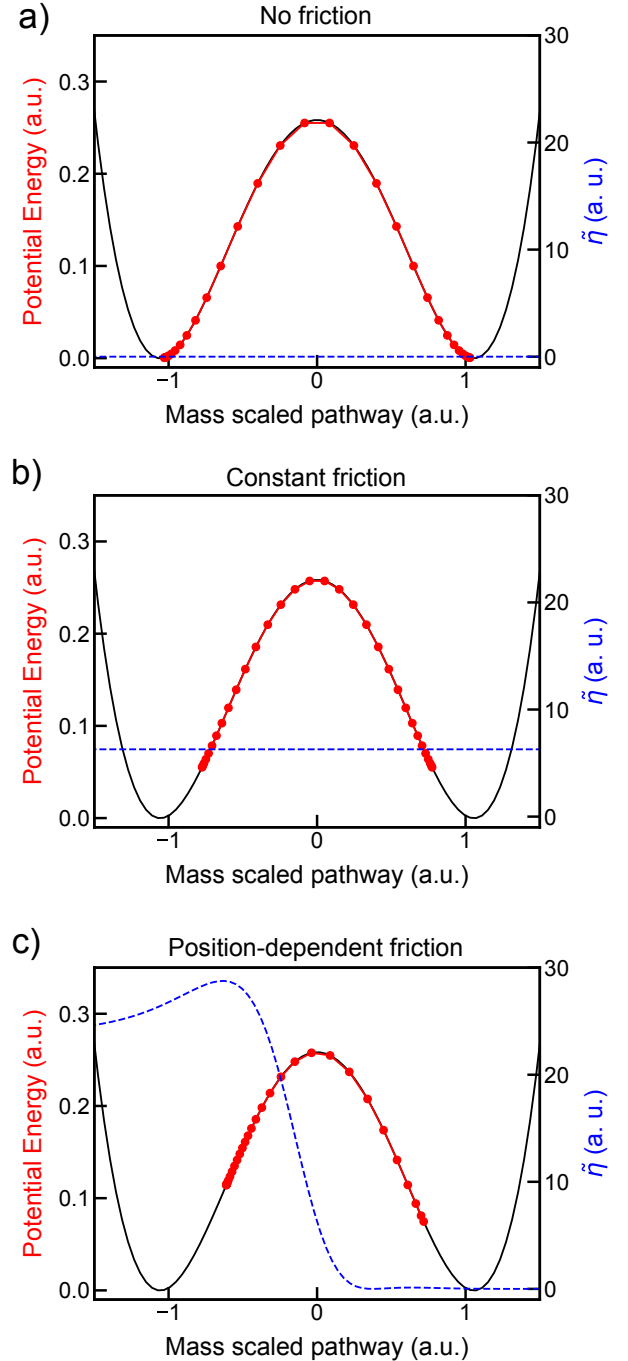


FIG. 9. Instanton pathways obtained in double-well (DW) potential with a) no friction, b) constant friction and c) position-dependent friction. The instanton pathways, potential energy surface and friction profiles, $\tilde{\eta}$, are depicted as red dotted lines, black solid lines and blue dashed lines, respectively. The analytical expression of the potential and friction profiles can be found in Ref. [98].

possibility of *dynamical materials design*. [128, 129]

Many of these phenomena rely on the existence of anharmonic coupling between different vibrational modes

that lead to the so-called nonlinear effects in vibrational dynamics.[130, 131] A popular approach to simulate these experiments and capture the associated nonlinear dynamics is based on the electric dipole approximation (EDA). Within EDA, one can further assume that the changes induced by the electric field \mathcal{E} on the electronic structure are not significant, and expand the electric enthalpy function of a system around the vanishing-field condition up to first order. This leads to the following expression for the (external field dependent) potential energy

$$U(\mathcal{E}, \mathbf{q}) \simeq V(\mathbf{q})|_{\mathcal{E}=0} - \mathcal{E} \cdot \boldsymbol{\mu}(\mathbf{q}). \quad (5)$$

where $\boldsymbol{\mu}$ is the dipole moment of the system in the absence of the electric field and \mathbf{q} represents the atomic positions. Eq. 5 can be evaluated with a variety of theories. For example, when employing DFT, evaluating the expression above would require a full self-consistent convergence of the Kohn-Sham (KS) energy and the dipole corresponding to this converged electronic density. In periodic systems, the dipole would have to be expressed in terms of the system polarization, calculated with the Berry-phase formalism.[132]

Assuming a time-dependent electric field, $\mathcal{E}(t)$, the effect of the external field manifests itself on the nuclear dynamics through the nuclear forces, \mathbf{F} ,

$$\mathbf{F} = -\frac{\partial U(\mathcal{E}, \mathbf{q})}{\partial \mathbf{q}} = -\frac{\partial V(\mathbf{q})}{\partial \mathbf{q}} \Big|_{\mathcal{E}=0} + \mathcal{E}(t) \cdot \frac{\partial \boldsymbol{\mu}}{\partial \mathbf{q}}, \quad (6)$$

where the first term corresponds to the usual forces in the absence of an external field. The second term can be conveniently expressed in terms of the *dynamical charges*, or Born effective charges (BEC) $Z_{\alpha j}^*$, defined as,

$$Z_{\alpha j}^* = \frac{1}{e} \frac{\partial \mu_{\alpha}}{\partial q_j}, \quad (7)$$

where e is the elementary charge (1 in atomic units) $\alpha = x, y, z$ runs through the Cartesian components of the total dipole and $j = 1, \dots, 3N$ runs through the degrees of freedom of the system. With this definition, the last term in Eq. 6, henceforth \mathbf{F}^{ext} , reads

$$F_j^{\text{ext}}(t) = \sum_{\alpha=x,y,z} \mathcal{E}_{\alpha}(t) Z_{\alpha j}^*. \quad (8)$$

For a fixed atomic configuration, the BEC can be computed by finite differences of the dipole values with respect to the atomic positions. In the context of DFT, it is also possible to exploit density functional perturbation theory (DFPT).[133, 134]

The i-PI implementation for driven vibrational motion is based on the definition of a time-dependent integrator for the equations of motion, called `EDAIIntegrator`, built on top of the already implemented integrators. The role of this integrator is simply to add $\mathbf{F}^{\text{ext}}(t)$ to the momenta within the Verlet algorithm. This was implemented in a

new *motion* class of i-PI, called `DrivenDynamics`, which inherits all the attributes and methods of the already implemented `Dynamics` class.

We implemented a plane-wave linearly-polarized electric field with a Gaussian envelope function, of the following form,

$$\mathcal{E}(t) = \mathcal{E}_{\text{amp}} \cos(\omega t) \frac{1}{\sigma\sqrt{2\pi}} e^{-\frac{(x-m)^2}{2\sigma^2}} \quad (9)$$

where ω is the frequency of the plane-wave, \mathcal{E}_{amp} is the polarization vector of the electric field, and m and σ^2 are the mean and variance of the Gaussian envelope function, respectively. Other types of field profiles can be added straightforwardly.

The BECs and dipoles are communicated by the client at every new nuclear configuration through the i-PI `extras` field as a JSON formatted string. An example of the communication of such a client is provided in the Python driver code distributed with i-PI (see `driverdipole`). Alternatively, BECs can be provided as a `txt` file and kept fixed during the dynamics.

An example of the section `motion` to run dynamics driven by a Gaussian-enveloped electric field with fixed BECs reads

```
<motion mode='driven_dynamics'>
  <driven_dynamics mode='eda-nve'>
    <timestep units='femtosecond'> 0.3 </timestep>
    <efield>
      <amp units='atomic_unit'> [0,5e-2,0] </amp>
      <freq units='thz'> 115 </freq>
      <peak units='picosecond'> 0.2 </peak>
      <sigma units='picosecond'> 0.05 </sigma>
    </efield>
    <bec mode='file'> bec.txt </bec>
  </driven_dynamics>
</motion>
```

In this example, the `amp`, `freq`, `peak`, and `sigma` tags refer to \mathcal{E}_{amp} , ω , m and σ as defined in Eq. 9, respectively. The file `bec.txt` contains a 2D array of shape $(3N, 3)$. The columns correspond to the Cartesian components of the dipole and the rows to the degrees of freedom j in Eq. 7. The current implementation only supports the NVE ensemble, but will soon be ported to other ensembles.

As a benchmark example, a single water monomer has been driven using fixed BECs and the Partridge-Schwenke water model.[135] The parameters adopted for the electric field are the ones shown in the input example above. The resulting trajectory, initialized with vanishing velocities has then been projected along the 3 vibrational modes of the system, which have been computed using the harmonic vibrational analysis provided by i-PI. The vibrational modes are shown in Fig. 10a. The oscillating frequency of the field at around 3836 cm^{-1} (115 THz) was chosen to be resonant with the symmetric-stretch mode. Fig. 10b shows the energy given by the sum of the three harmonic vibrational mode energies (E_{bend} , $E_{\text{sym.stretch}}$, $E_{\text{asym.stretch}}$). E_{anharm} is computed as

the difference between the total energy and the sum of the harmonic energies. The profile of the applied field is also shown in Fig. 10. As expected, the resonant vibrational mode is excited and the energy of the system increases while the driving field assumes non-negligible values. Afterwards, the field decays to zero but the system remains excited due to the lack of a dissipation mechanism. By comparing the different components of the energy, it is evident that the harmonic contribution is dominated by the symmetric-stretch mode and that the anharmonicity plays a relatively minor role in this simple example.

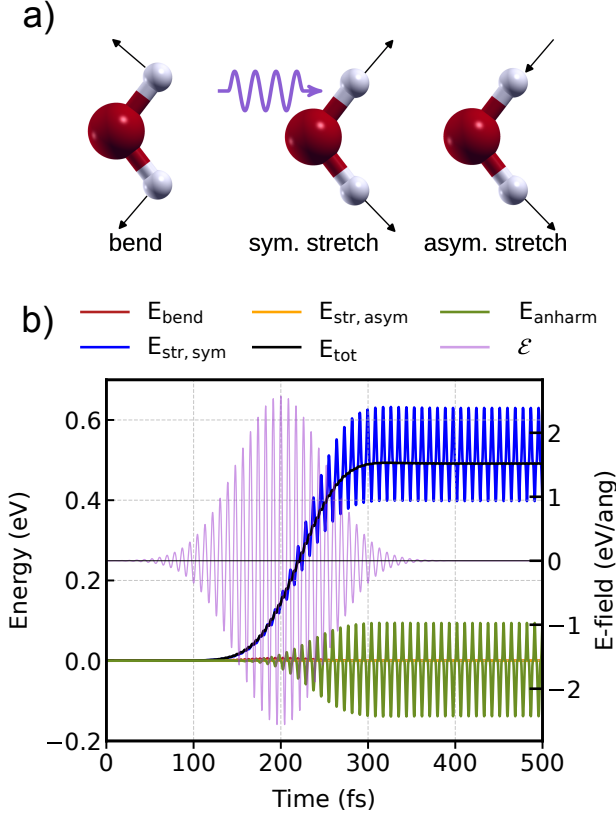


FIG. 10. (a) Vibrational modes of a water monomer: bending E_{bend} , symmetric-stretch $E_{\text{str, sym}}$, and asymmetric-stretch $E_{\text{str, asym}}$. (b) Contributions to the total energy along a driven trajectory. Time series of the harmonic contribution to the energy of different vibrational modes, the total energy E_{tot} , and the anharmonic contribution E_{anharm} of a water monomer along a driven trajectory. The $E_{\text{str, sym}}$ mode is resonant with the applied electric field \mathcal{E} (shown in purple).

C. Ensemble models and error estimation

This version of i-PI implements error estimation for MLIPs based on ensembles. The idea is that, for each configuration A , multiple potentials $V^{(k)}(A)$ are computed, together with the associated forces. The simulation is then evolved based on the mean of the en-

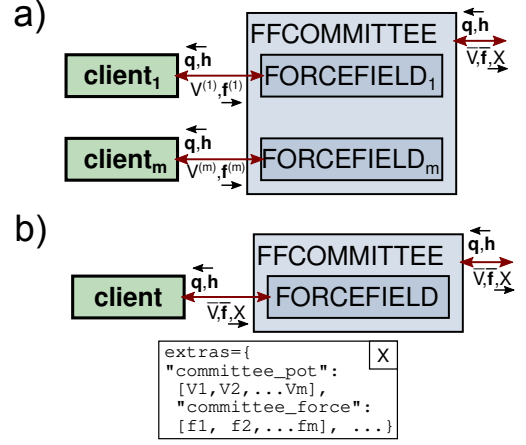


FIG. 11. Schematic representation of the implementation of the *FFCommittee* class, that combines the members of an ensemble model to evaluate the mean potential and force, that are used to propagate the dynamics. The statistics of the ensemble are stored in a JSON-formatted *extras* string, depicted in the figure with the *X* label. This class can handle two types of models. The first one, depicted in panel a, works by collecting data from one forcefield per committee member, which is suitable for fully independent models. Alternatively, a single forcefield can compute all ensemble members, returning them to i-PI as a JSON string with the same syntax (panel b), which is then used to compute the error. This second mode is particularly suitable for shallow models with a high degree of weight sharing.

semble $\bar{V}(A) = \frac{1}{n_{\text{ens}}} \sum_k V^{(k)}(A)$, where n_{ens} is the number of potentials in the ensemble, and the error is estimated as the standard deviation $\sigma^2(A)$. While, in general, ensemble approaches entail a large computational overhead because n_{ens} potentials have to be evaluated at each time step, there are cases in which this overhead can be largely avoided, as e.g. when employing linear or kernel methods,^[136] or when applying a high-level of weight sharing between different neural networks e.g. using a “shallow-ensemble” on the last-layer.^[100, 137–141] i-PI provides two alternative modes to simulate nuclear (thermo)dynamics including ensemble-based uncertainty estimates, depending on the characteristics of the underlying framework.

The first entails independent models that are run as separate clients, by specifying multiple socket connectors as part of a `<ffcommittee>` tag. For instance,

```
<ffcommittee name="my_committee">
  <ffsocket name='driver-1'>
  [...]
</ffsocket>
  <ffsocket name='driver-2'>
  [...]
</ffsocket>
  [...]
</ffcommittee>
```

The associated class takes care of collecting potentials, forces and stresses from the various sockets and averaging them. Even though a `ffcommittee` section contains multiple sockets, one should use a single `<force>` block referring to the name of the committee (`my_committee` in this example) in the definition of the system. A linear committee calibration scaling [136] can also be applied with the keyword `<alpha>`.

In the second mode, which is suitable when using a shallow ensemble model with weight sharing, a single client computes all the ensemble members. In this case, the client passes the average energies, forces and virials to i-PI in the standard way and also passes the ensemble information as a JSON string into the `extras` field. The string contains the list of potentials, forces, and virials into fields named `committee_pot`, `committee_force`, `committee_virial`. We provide a reference implementation of such a client in the FORTRAN driver distributed with i-PI. It is then sufficient to specify a single client in the committee section

```
<ffcommittee name="my_committee">
  <ffsocket name='driver'>
    [...]
  </ffsocket>
  <parse_json> True </parse_json>
</ffcommittee>
```

and to activate the flag `parse_json` that instructs the committee class to parse the ensemble data out of the string. Also in this case, the `forces` section should refer to "my_committee" and not to the name of the inner forcefield.

For both modes, committee potentials, forces, as well as the computed uncertainty, are collected into an `extras` dictionary corresponding to the same schema used for the JSON string. The different diagnostics can then be printed out using the generic output features, e.g. specifying `extra_type='committee_pot'` to print the energies of all members of the ensemble.

The committee forcefield implements a rudimentary active-learning mechanism. By specifying an output filename and an error threshold, every structure with a predicted uncertainty above the threshold encountered at any point of a calculation will be stored so it can be used to improve the MLIP model in an iterative manner. It is also possible to build a *weighted baseline* model,[142] in which one forcefield, whose name is specified in the `<baseline_name>` flag, is interpreted as a reference potential, to which the model described by a committee is added as a correction. The baseline is assumed to have a constant uncertainty σ_{base} , that can be set with the option `<baseline_uncertainty>`. Rather than simply computing the overall potential as $V = V_{\text{base}} + \bar{V}$, the weighted baseline potential is computed as

$$V(A) = V_{\text{base}}(A) + \frac{\sigma_{\text{base}}^2}{\sigma_{\text{base}}^2 + \sigma^2(A)} \bar{V}(A) \quad (10)$$

which uses the correction when the predicted error is

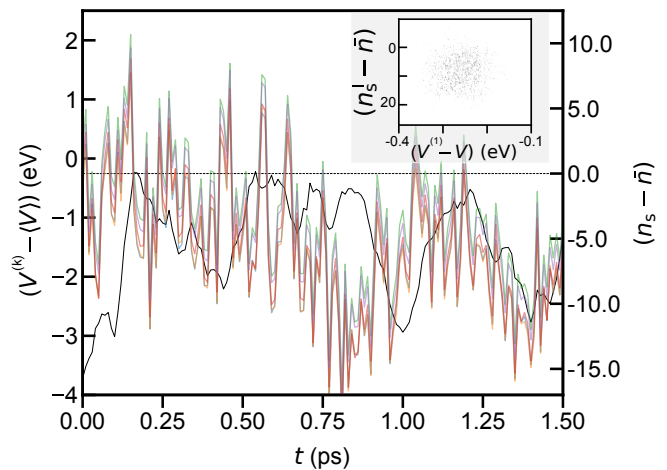


FIG. 12. Trajectories of the various energy predictions of the DPOSE committee model and of the order parameter that determines the pinning potential (11). The inset shows the near-Gaussian correlation plot between the order parameter and the deviation of one of the ensemble members from the mean potential.

smaller than the baseline error, and switches to the more reliable (although less accurate for structures that are well-predicted by the committee) baseline potential.

1. Computing the solid-liquid chemical potential for water

We discuss a representative example of the use of `ffcommittee` to compute errors in on the solid-liquid chemical potential $\Delta\mu$ for an ice/water system, that showcases several of the advanced features in i-PI. This type of simulation can be used to estimate the melting point of water T_m , by repeating the procedure at different temperatures and finding the temperature at which $\Delta\mu = 0$. As shown in Ref. 142, once a collection of $\Delta\mu$ values associated with the different ensemble members has been obtained, it is easy to determine the error on T_m by ensemble propagation.

For this example, we use a Behler-Parrinello-style neural network,[143] based on smooth-overlap of atomic positions (SOAP)[144] features and trained on the dataset of Ref. 14. The model generates an ensemble of 5 energy predictions, differing only by the last-layer weights and trained by optimizing the negative log likelihood following the direct propagation of shallow ensembles (DPOSE) protocol.[100] We run a simulation with 336 water molecules, arranged in an elongated simulation cell containing coexisting water and ice. A restraining *pinning potential* to an anchor point, \bar{n} ,

$$V_{\text{pin}}(A) = \frac{1}{2}k(n_S(A) - \bar{n})^2 \quad (11)$$

is applied using a suitable collective variable that estimates the number of molecules in a solid-like environment, $n_S(A)$, [145] as implemented in PLUMED.[146] At

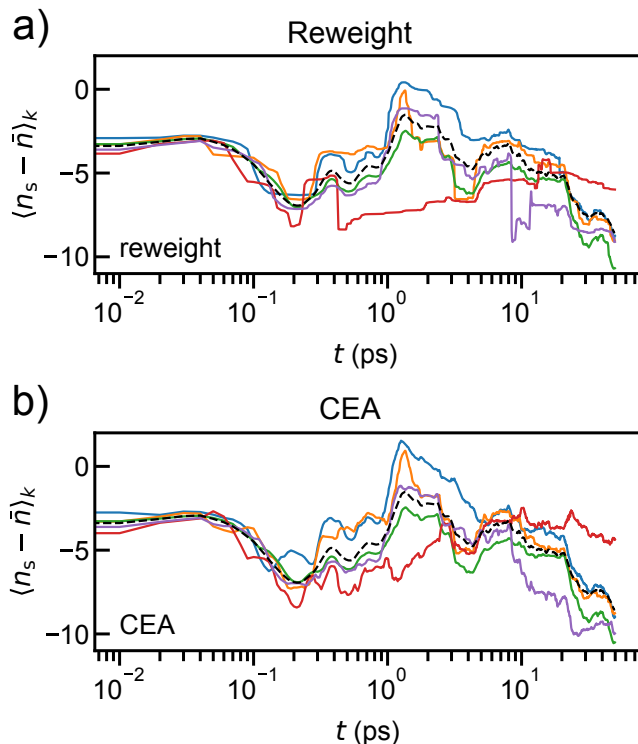


FIG. 13. Cumulative sums of the reweighted mean $\langle n_S - \bar{n} \rangle_k$ computed using the k -th ensemble member. The dashed black line indicates the cumulative average of n_S computed without reweighting. Panel a) shows the average computed with Boltzmann reweighting while panel b) uses a statistically-better-behaved cumulant expansion approximation (CEA).

the melting point, the potential restraints the solid fraction to the target value \bar{n} , whereas away from equilibrium the mean deviation is proportional to the solid-liquid molar free-energy difference, $\Delta\mu \propto \langle n_S(A) - \bar{n} \rangle$. Further details on the setup can be inferred from the example files included in the `demos/ensemble-deltamu` folder. It should be noted that both size and duration of the simulations are insufficient to obtain a converged estimate of the melting point, as this is only intended as a demonstrative example.

Fig. 12 shows a small segment of a trajectory obtained with the DPOSE model. The mean potential undergoes thermal fluctuations, and the ensemble of predictions has a varying spread along the trajectory. Similar to what was observed in Ref. 100, the members of the ensemble differ mostly by a rigid shift, reflecting a systematic bias in the prediction of the potential. Meanwhile, the order parameter fluctuates about a value that is slightly below the target, indicating that the simulation temperature (290 K) is above the melting point for this water model – at least for this under-converged supercell size. There is no obvious pattern in the correlation between the total potential energy and the order parameter: at this temperature, and for such a comparatively small system, random fluctuations dominate over the enthalpy change

associated with the changes in the solid fraction. Importantly, the cross-correlations between the solid fraction and the ensemble potential shift ($V^{(k)}(A) - \bar{V}(A)$) show approximately Gaussian behaviour (see inset in Fig. 12). This simplifies the estimation of the average deviation $\langle \langle n_S(A) - \bar{n} \rangle \rangle$ from a single trajectory driven by \bar{V} . The basic idea is to use Torrie-Valleau reweighting,[147] i.e. weighting each snapshot by $e^{-\beta(V^{(k)}(A) - \bar{V}(A))}$. As shown in Fig. 13, the cumulative averages computed with the different weighting factors converge to different values – providing an ensemble of predictions for $\langle n_S - \bar{n} \rangle_k$. The sharp, sudden changes in the cumulative average reflect the occurrence of very large weighting factors, that occur whenever the deviations of individual predictions from the mean potential are large relative to $k_B T$. The resulting statistical inefficiency[87] would become worse as the system size is increased, eventually making the procedure completely ineffective. Following Ref. 142, one can use instead a cumulant expansion approximation (CEA) that estimates reweighted average under the assumption that the target observable and the potential are joint Gaussians, and yields

$$\langle n_S \rangle_k \approx \langle n_S \rangle - \beta [\langle n_S (V^{(k)} - \bar{V}) \rangle - \langle n_S \rangle \langle (V^{(k)} - \bar{V}) \rangle]. \quad (12)$$

This approximation introduces a systematic error because the distribution is *not* exactly Gaussian, but as can be seen in Fig. 12, the qualitative behaviour reflects the one seen for the direct reweighting. The statistical error is well-behaved also for large simulations, making the CEA a more generally applicable strategy. We provide a commented example to perform this kind of simulation in the `demos/ensemble-deltamu`; the post-processing needed to evaluate the reweighted averages is implemented in the `i-pi-committee-reweight` script. By repeating the simulation at different temperatures one can determine the temperature dependence of $\Delta\mu$ for each ensemble member separately, and use the separately-computed values of T_m to estimate the error in the determination of the melting point. It is worth noting that in Ref. 142 the melting point was determined to be 290 ± 5 K, with a setup similar to the one discussed here, but using a deep ensemble of models, fitted on the same dataset. This estimate is consistent with our observation that $\langle n_S - \bar{n} \rangle$ at 290 K is very close to zero. The discrepancy with Ref. 14, where the classical melting point for the reference DFT was determined by free-energy perturbation to be at ≈ 275 K can be attributed to finite-size effects, that tend to de-stabilize the liquid and increase the melting point.

D. Cavity Molecular Dynamics for Polaritonics

For molecules confined in optical cavities, molecular transitions may form polaritons, the hybrid light-matter states, with cavity photon modes.[148–152] Of particular interest is the vibrational strong coupling regime,[153, 154] in which vibrational polaritons are

formed when a molecular vibrational mode is near resonant with an IR cavity photon mode. Under vibrational strong coupling, many molecular properties, including chemical reaction rates and energy transfer rates, can be significantly modified in the liquid phase.[155–157] For a better understanding of these exciting experiments, both the molecules and the cavity photons need to be propagated self-consistently with realistic parameters. This requirement is beyond the scope of standard molecular dynamics schemes, whereby the time-dependent dynamics of the photon field are not explicitly propagated.

The i-PI package provides an efficient method for simulating vibrational strong coupling: the CavMD approach.[92, 93] Within the framework of CavMD, both nuclei and cavity photons in the infrared domain are treated classically, propagated by the following light-matter Hamiltonian under the ground electronic state: $H_{\text{QED}} = H_{\text{M}} + H_{\text{F}}$, [92, 158] where H_{M} denotes the standard molecular Hamiltonian composed of the kinetic and potential terms, and

$$H_{\text{F}} = \sum_{\mathbf{k}, \lambda} \frac{\tilde{p}_{\mathbf{k}, \lambda}^2}{2m_{\mathbf{k}, \lambda}} + \frac{1}{2} m_{\mathbf{k}, \lambda} \omega_{\mathbf{k}, \lambda}^2 \left(\tilde{q}_{\mathbf{k}, \lambda} + \frac{\tilde{\varepsilon}_{\mathbf{k}, \lambda} d_{\lambda}}{m_{\mathbf{k}, \lambda} \omega_{\mathbf{k}, \lambda}^2} \right)^2. \quad (13)$$

Here, $\tilde{p}_{\mathbf{k}, \lambda}$, $\tilde{q}_{\mathbf{k}, \lambda}$, $\omega_{\mathbf{k}, \lambda}$, and $m_{\mathbf{k}, \lambda}$ denote the momentum, position, frequency, and auxiliary mass for the cavity photon mode defined by a wave vector \mathbf{k} and polarization direction $\boldsymbol{\xi}_{\lambda}$ with $\mathbf{k} \cdot \boldsymbol{\xi}_{\lambda} = 0$. For example, when the cavity is placed along the z direction, $\lambda = x, y$. d_{λ} is the electronic ground-state dipole moment for the molecular system projected along the direction of $\boldsymbol{\xi}_{\lambda}$, and $\tilde{\varepsilon}_{\mathbf{k}, \lambda}$ represents the effective light-matter coupling strength.

The basic implementation strategy of CavMD is as follows. The cavity photon modes are stored in i-PI as **L** (light) atoms. The coordinates and velocities of both the nuclei and the cavity photon modes are propagated in i-PI. A new *FFCavPhSocket* class, which inherits from the original *FFSocket* class, evaluates the forces of both the nuclei and the cavity photon modes. Similar to *FFSocket*, *FFCavPhSocket* calls external client codes to evaluate the nuclear forces associated with H_{M} , via the socket interface. After obtaining this component of the total forces, *FFCavPhSocket* performs additional calculations to obtain the photonic forces as prescribed by Eq. 13. Because this implementation encapsulates the cavity-related calculations within the *FFCavPhSocket* class, many advanced features in i-PI, including RPMD, [92] and ring-polymer instantons, can be directly applied to study vibrational strong coupling without additional modifications of the i-PI code.

The CavMD implementation was used to simulate the IR spectra of liquid water under vibrational strong coupling.[92] The key i-PI input section to simulate vibrational strong coupling is as follows:

```
<ffcavphsocket name='lammps' mode='unix'>
<address>h2o-cl-cavmd</address>
<apply_photon> True </apply_photon>
```

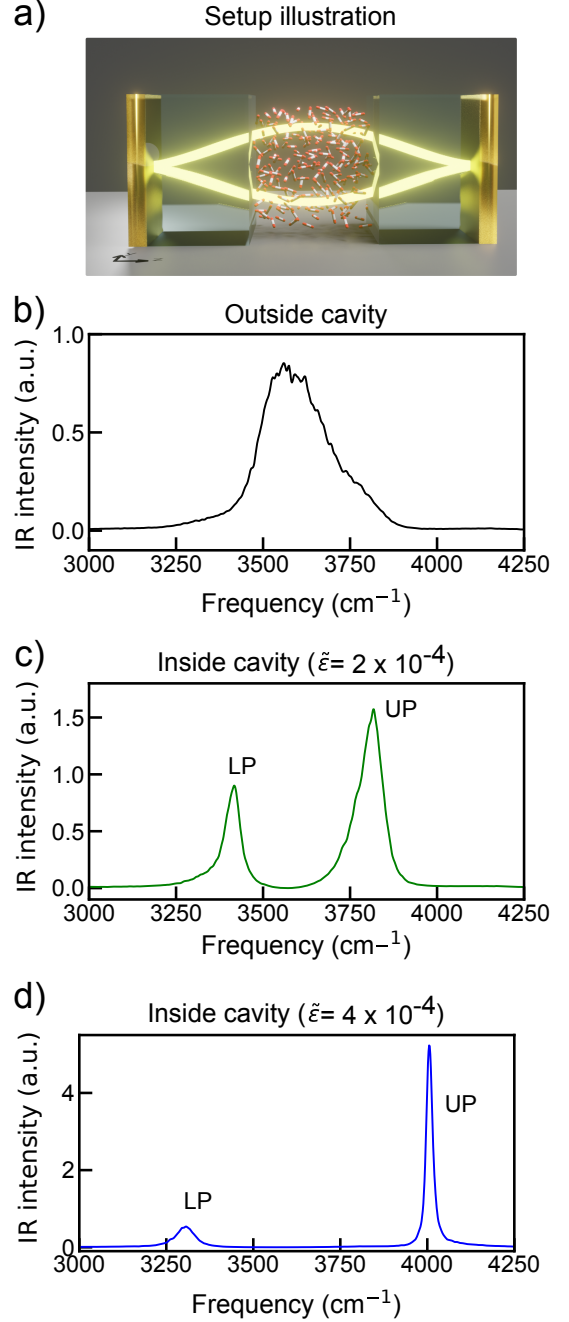


FIG. 14. CavMD simulations: Panel (a) illustrates the simulation setup of CavMD, whereby a large ensemble of molecules is confined in an optical cavity under vibrational strong coupling. The rest of the panels are adapted from Ref. 92 and show the IR spectra of the OH stretch mode of liquid water outside the cavity and inside the cavity with different light-matter coupling strength, $\tilde{\varepsilon}$. LP and UP stand for lower and upper polariton, respectively.

```

<EO> 4e-4 </EO>
<omega_c units='inversecm'> 3550.0 </omega_c>
<charge_array> [...] </charge_array>
</ffcavphsocket>

```

In the *FFCavPhSocket* section above, a cavity mode with frequency $\omega_c = 3550 \text{ cm}^{-1}$ was coupled to liquid water with an effective light-matter coupling strength $\tilde{\epsilon} = 4 \times 10^{-4}$ a.u. Under the default setting, the cavity mode is polarised along both the x and y directions. The partial charges of all molecular atoms are given in the *charge_array* section of *FFCavPhSocket*, and are used to evaluate the molecular dipole moment in Eq. (13). In Fig. 14 we show a schematic picture of the setup along with the IR spectra of water inside and outside the cavity. As shown in Fig. 14c, via classical CavMD simulations, the wide OH band of liquid water splits into a pair of polariton states, the upper polariton (UP) and the lower polariton (LP). Beyond this study, CavMD was also used to explore novel energy transfer and chemical reaction pathways under vibrational strong coupling. [159–161]

V. SHOWCASE OF ADVANCED SIMULATION SETUPS

A. Path Integral Coarse-Grained Simulations

The imaginary-time path integral approach provides a rigorous framework for equilibrium time-independent properties but it doesn't give access to real-time quantum dynamics.[163] Nevertheless, it is possible to extract meaningful dynamical information from path integral simulations by making approximations to Matsubara dynamics.[164] Standard path-integral based methods for approximate quantum dynamics, (thermostatted) ring polymer molecular dynamics [74, 78] (RPMD) and centroid molecular dynamics [77] (CMD), can be shown to be approximations to Matsubara dynamics.[165] Unfortunately, both RPMD and CMD exhibit accuracy and cost limitations. For instance, in estimating the vibrational density of states, RPMD, CMD and variants [166–169] present artefacts such as unphysical shifted or broadened peaks.[166, 170] In addition, the computational overhead and impact of the artefacts become more pronounced with lowering temperature.

In their recent work, Musil *et al.* [79] introduce a machine learning framework to significantly enhance the accuracy and efficiency of approximating quantum dynamics based on path-integral simulations. This approach is closely related to CMD, which involves the classical time-evolution of a system on the centroid potential of mean force, effectively capturing nuclear quantum effects up to the fluctuations of the path integral centroid. This framework has two components: a temperature elevation (Te) ansatz and path integral coarse-graining simulations (PIGS). The Te ansatz addresses issues such as spurious redshift in CMD,

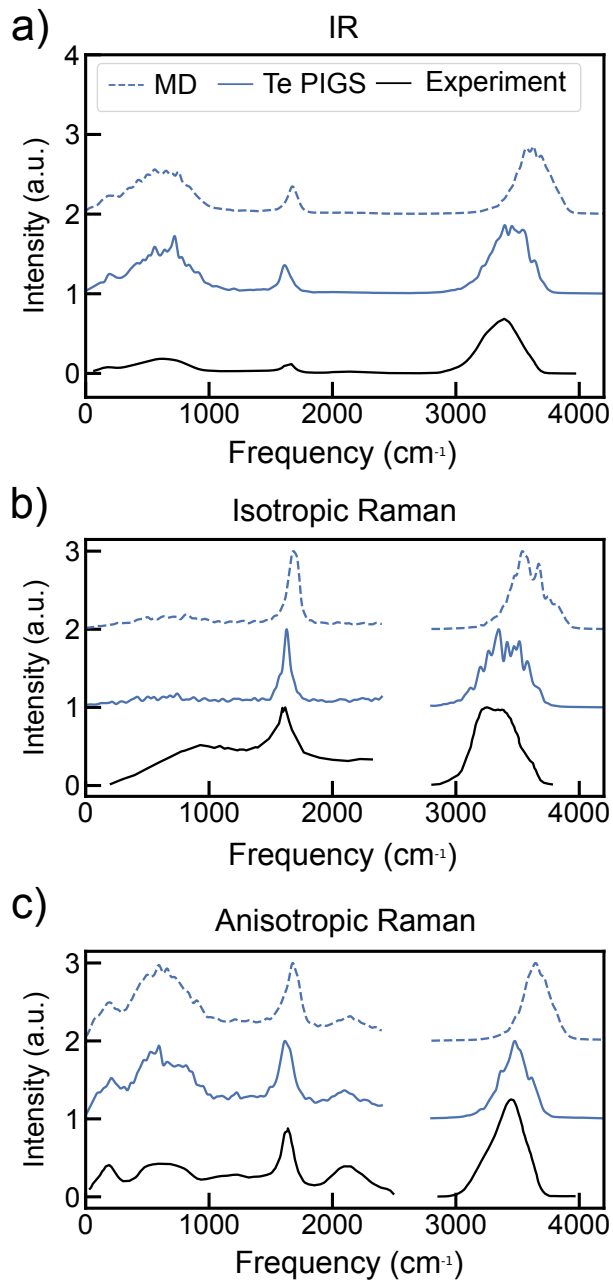


FIG. 15. IR, isotropic Raman, and anisotropic Raman vibrational spectrum of water at 300 K using the Te PIGS method. Adapted from Ref. 162.

resulting in notable improvements in the accuracy of vibrational spectra in bulk [162] and interfacial [171] systems compared to existing methodologies. Meanwhile, PIGS enables the machine learning of the centroid potential of mean force using state-of-the-art machine learning potentials. Thus, the Te PIGS approach allows accurate modelling of quantum dynamics in condensed phase systems via simple and inexpensive classical MD on a machine learning potential.

This approach is easily implemented using the flexible functionality of i-PI as demonstrated for various vibrational spectroscopic observables of liquid water (see Fig. 15) using the MACE-OFF23(S) general organic machine learning potential.[162] For a given potential energy surface $V(\mathbf{q})$, training the Te PIGS machine learning potential requires data from an elevated-temperature simulation, such as the centroid positions $\bar{\mathbf{q}} = \frac{1}{P} \sum_{j=1}^P \mathbf{q}^{(j)}$, the mean force acting on the centroid, $\mathbf{f}^{\text{CMD}} = -\frac{1}{P} \sum_{j=1}^P \frac{\partial V(\mathbf{q}^{(j)})}{\partial \mathbf{q}^{(j)}}$, and the physical force acting on the centroid, $\mathbf{f} = -\frac{\partial V(\bar{\mathbf{q}})}{\partial \bar{\mathbf{q}}}$. In this example from Ref. 162, the elevated temperature is set to $T_e = 500\text{K}$ and the centroid potential of mean force is fit from a 10 ps long path integral simulation requiring just 8 replicas, with the centroid positions and forces sampled every 10 fs (20 timesteps). The centroid positions and forces can be printed out as follows:

```
....
<trajectory filename='xc' format='xyz'
stride='20'> x_centroid </trajectory>
<trajectory filename='fc' format='xyz'
stride='20'> f_centroid </trajectory>
...
```

To calculate the physical force acting on the centroid positions, we perform a “replay” simulation, which allows the calculation and output of properties or trajectory information on a list of centroid positions using:

```
...
<trajectory filename='for' format='xyz'
stride='1'> forces </trajectory>
...
<motion mode='replay'>
  <file mode='xyz'> simulation.xc.xyz </file>
</motion>
...
```

The Te PIGS machine learning potential can be developed using standard packages like `n2p2` [172], `nequip` [173], `mace` [174] using so-called “delta learning” by regressing on the centroid positions as the input and the difference between \mathbf{f}^{CMD} and \mathbf{f} as the target.

Performing a Te PIGS simulation only requires classical molecular dynamics on the sum of the potential energy surface $U(\mathbf{q})$ and the Te PIGS machine learning potential. This can be done in i-PI by exploiting the modularity of forces. As shown in the following snippet, this setup requires to define two forcefield sockets for the potential energy surface and the Te PIGS machine learning potential:

```
...
<ffsocket name='PES' mode='unix'>
  <address> driver.1 </address>
</ffsocket>
<ffsocket name='TEPIGS' mode='unix'>
  <address> driver.2 </address>
```

```
</ffsocket>
...
```

The addition of the potentials along with the calculation of all derivatives like the force and stress is done under the hood by defining the forces of the system class comprising two force components that communicate with the forcefield sockets:

```
...
<forces>
  <force forcefield='PES' weight='1.0'>
</force>
  <force forcefield='TEPIGS' weight='1.0'>
</force>
</forces>
...
```

B. 2D IR-Raman spectra of liquid water

Nonlinear, multi-time response functions are associated with different flavours of time-resolved and multidimensional spectroscopic techniques.[175] Here, we show an example provided in i-PI *demos*, that simulates the two-dimensional IR-Raman spectrum of liquid water in which the sample interacts first with two mid- or far-IR pulses through a dipole interaction and then with a near-IR or visible pulse through a Raman process.[176, 177] The spectrum is obtained as a two-dimensional Fourier sine transform of the two-time response function

$$R(t_1, t_2) = -\frac{1}{\hbar^2} \langle [\hat{\alpha}(t_1 + t_2), \hat{\mu}(t_1)], \hat{\mu}(0) \rangle \quad (14)$$

where $\hat{\alpha}$ is the polarizability operator and $\hat{\mu}$ the dipole moment. The example presented in `demos/2D-IR-Raman` implements the equilibrium-nonequilibrium RPMD method of Refs. 95-96, which approximates the true quantum-mechanical response function (14). As a special case when the number of ring-polymer beads P is 1, the method corresponds to the MD approach of Hasegawa and Tanimura.[94] In passing, we note that other methods based on imaginary-time path integrals have been reported to calculate non-linear response functions using approximations to fully-symmetrized multi-time Kubo correlation functions.[178-180]

The equilibrium-nonequilibrium method requires sampling the initial distribution as in a typical PIMD simulation and running three trajectories for each initial phase-space point (q_0, p_0) —one backward equilibrium trajectory along which we evaluate the dipole moment and two nonequilibrium trajectories that are initialized with a momentum kick, i.e., starting from $(q_{\pm,0} = q_0, p_{\pm,0} = p_0 \pm \varepsilon \mu'(q_0)/2)$ (see schematics in Fig. 16a). The two-time response function is then computed as

$$R^{(2)}(t_1, t_2) = \frac{\beta}{\varepsilon} \langle [\alpha(q_{+,t_2}) - \alpha(q_{-,t_2})] \dot{\mu}(q_{-t_1}) \rangle, \quad (15)$$

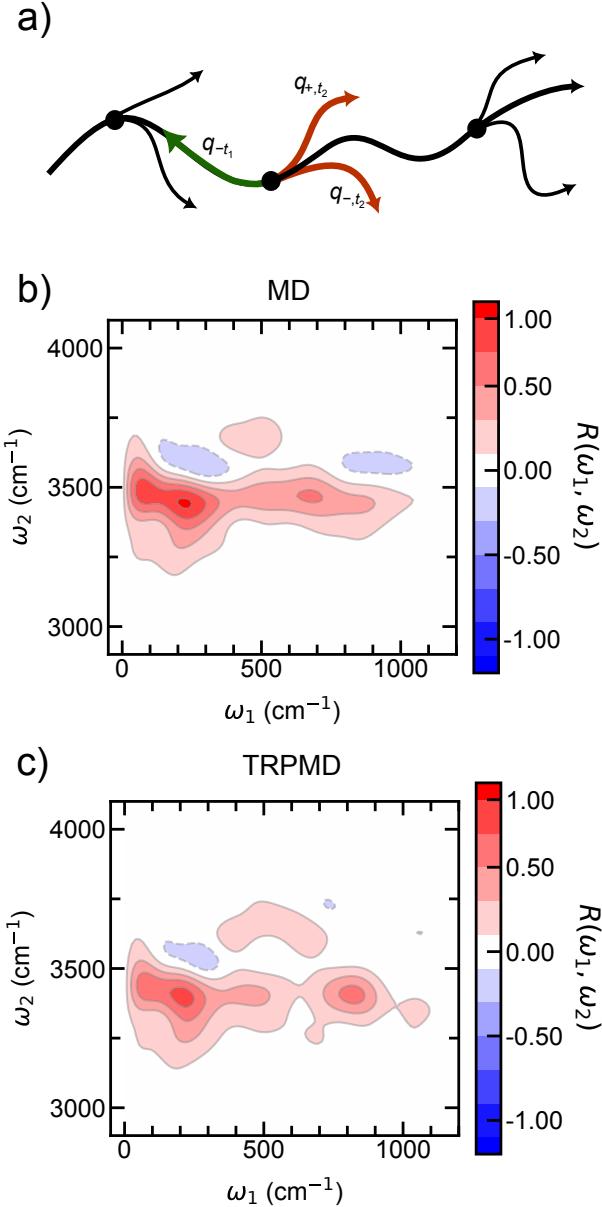


FIG. 16. Two-dimensional IR-Raman spectroscopy: Panel (a) shows the schematic of the equilibrium-nonequilibrium (RP)MD approach (see text). Panel (b) and (c) depict the frequency-dependent response function corresponding to the two-dimensional THz-IR-Raman (also called THz-IR-visible [176]) spectrum of liquid water, computed using classical MD and TRPMD, respectively. Figure adapted from Ref. 96.

where $\langle \cdot \rangle$ now represents a classical average over the ring-polymer equilibrium distribution at inverse temperature β . ε is a parameter that controls the magnitude of the perturbation (“kick”) applied to the nonequilibrium trajectories. Position-dependent operators $\alpha(q)$ and $\mu(q)$ in Eq. (15) are evaluated as averages over P beads of the ring polymer, same as in the case of linear RPMD correlation functions.[74]

The evaluation of nonequilibrium trajectories, two-time response function, and two-dimensional spectrum is implemented in the scripts provided in `demos/2D-IR-Raman`. The `noneqm-traj.py` script uses checkpoint files and z -dipole nuclear gradients stored along a longer RPMD trajectory to run multiple shorter nonequilibrium trajectories (see Fig. 16a). In this way, the long RPMD trajectory serves both for sampling initial conditions and computing the response function. To properly sample the canonical ensemble, the whole calculation is typically repeated with independent RPMD trajectories. The `noneqm-response.py` script then computes the response function by reading in the dipole moments and polarizabilities along the long equilibrium trajectory and nonequilibrium trajectories. Finally, two-dimensional IR-Raman spectroscopy strongly depends on the nonlinearity of the polarizabilities and dipole moments (electrical anharmonicity). To study these and other phenomena that are sensitive to such nonlinearities, we implemented a simple truncated dipole-induced-dipole model for water in i-PI’s internal Fortran driver (option `-m water_dip_pol`). Classical and TRPMD two-dimensional IR-Raman spectra of liquid water at 300 K are displayed in Fig. 16b showing that NQEs play a minor role in this observable. Overall, this example illustrates how minor scripting and modifications outside of the core i-PI code can be used to implement new methods and study various types of dynamical properties.

C. Melting of Charge Density Waves in 2D Materials

Downfolded lattice models aim to reduce the complexity of the full electronic problem by treating only a few low-energy electronic states (around the Fermi energy) explicitly and defining a simplified Hamiltonian where all other high-energy states are integrated out.[181] The parameters required for this dimensionality reduction can be obtained directly from *ab initio* calculations. There are several ways to include the effect of screening of the high-energy electrons on the several interaction terms related to the explicit degrees of freedom of the downfolded Hamiltonian,[182] and making appropriate choices in this respect is necessary to reproduce the fully *ab initio* potential energy surface of certain materials.[19]

i-PI has recently been employed in this context, through its new interface with the `elphmod` code.[48] With `elphmod`, it is possible to set up downfolded models for the electronic interactions and for the electron-nuclear interactions, the latter being far less common to find in literature. Having access to the nuclear degrees of freedom in the Hamiltonian makes it possible to calculate nuclear forces efficiently, in the order of milliseconds per MD step per atom.[19]

In connection with i-PI, this capability allows the simulation of different types of molecular dynamics with such downfolded models. While machine-learning potentials

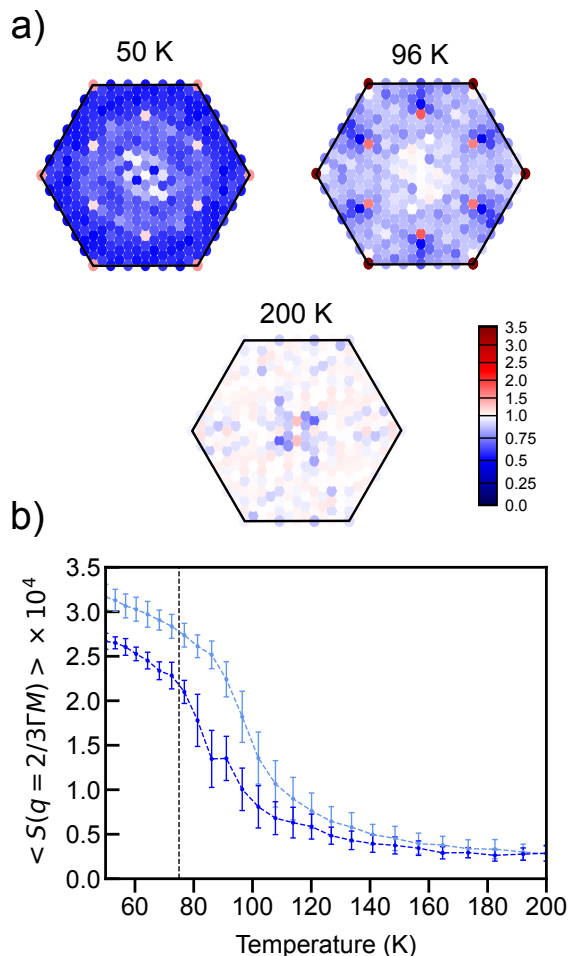


FIG. 17. (a) Ratio of structure factors S_{CL}/S_{PI} from classical and path integral MD performed on a 18×18 supercell of monolayer 1H-TaS₂. A value close to 1 (indicated in white) corresponds to minimal differences between classical and quantum simulations. The peaks at $\mathbf{q} = 2/3\Gamma M$ and $\mathbf{q} = K$ for $T = 50$ K are characteristic of the 3×3 CDW phase. (d) Temperature-dependent structure factor $\langle S(\mathbf{q}) \rangle_T$ at the characteristic CDW wavevector $\mathbf{q} = 2/3\Gamma M$ obtained from classical MD replica-exchange MD (light blue) and path integral replica-exchange MD (blue). The experimental value (for the bulk) is represented by the vertical black dashed line. The shift of the inflection point of the PIMD curve toward the experimental value is due to nuclear quantum effects. Figure and caption adapted from Ref. 19, with permission.

could play a similar role, there is an undeniable added value of physical interpretability when employing these models. Moreover, even if downfolded models cannot be applied to all types of materials, for suitable systems they are straightforward to parametrize.

In Ref. [19], large-scale replica-exchange and path-integral replica exchange simulations were performed with the i-PI/e`lphmod` combination in order to study the charge-density-wave (CDW) phase transition in monolayer 1H-TaS₂. The downfolded model was obtained from

PBE density-functional theory calculations. In particular, the phase-transition between the 3×3 CDW and the symmetric structure was studied. We note that capturing the nuclear dynamics involved in such phase transitions calls for techniques that include non-perturbative anharmonic effects such as (PI)MD. In addition, as explicitly shown in Ref. [19], finite-size effects on the phase-transition are significant for small unit cells in these systems, calling for potentials that are efficient enough to allow the simulation of larger unit cells containing thousands of atoms.

Experimentally, the “melting” temperature of the 3×3 CDW in bulk TaS₂ is measured at around 75 K.[183] While the phase-transition temperature is not known for the monolayer, it is accepted that it should not strongly deviate from the bulk temperature. In panels a and b of Fig. 17, we show the ratio between classical and quantum \mathbf{q} -resolved structure factors and the intensity of the CDW 3×3 diffraction peaks with varying temperature, respectively. The inflection point of these curves is shown to correlate with a peak in heat capacity calculated from the simulations. Nuclear quantum effects decrease the transition temperature by around 20 K, bringing it in closer agreement with the experimental estimate.

Such simulations open the path for a closer analysis of particular phonon modes that contribute to the CDW phase transition, an analysis of the co-existence of different CDW phases at metastable regions, and the mapping of more complex CDW phase diagrams. Given the close connection between CDW phases and superconductivity, this is a promising field of study. An example on how to setup and run the `elphmod` code in connection with i-PI is included in the examples folders of the i-PI and the `elphmod` repositories.

VI. CONCLUSIONS

In this manuscript, we described the latest release of the i-PI code, a flexible and efficient framework for advanced atomistic simulations. We presented several new features implemented since the previous release, 5 years ago. Just as importantly, we discussed the efforts made by the core developers and contributors towards better code documentation and improved code stability and performance. In this regard, we showed extensive performance benchmarks demonstrating that i-PI’s current computational overhead is minimal when using state-of-the-art MLIPs for production simulations, and reported that the current version reduces between 2 and 10 times the overhead of several common setups. Considering also the availability of uncertainty quantification, that can be propagated from an ensemble of potentials to thermodynamic averages, i-PI is now an ideal companion for ML-powered atomistic simulations.

The ease by which new types of advanced simulations can be implemented, or even realized using the ability of i-PI to combine different forcefields and sampling al-

gorithms, is demonstrated by the breadth of examples we showed in this paper, including simulations coupled to external fields, sampling of bosonic statistics and the estimation of spectroscopic observables by approximate quantum dynamics. We hope that this manuscript encourages more researchers to contribute their algorithms into i-PI, or simply to find in i-PI a useful, reliable and friendly tool that facilitates incorporating advanced simulation techniques to realize complex and insightful simulations of matter.

ACKNOWLEDGMENTS

Y.L. has been funded by the Deutsche Forschungsgemeinschaft (DFG, German Research Foundation) project number 467724959. V.K. acknowledges support from the Ernest Oppenheimer Early Career Fellowship and the Sydney Harvey Junior Research Fellowship, Churchill College, University of Cambridge. V.K. is grateful for computational support from the Swiss National Supercomputing Centre under project s1209, the UK national high-performance computing service, ARCHER2, for which access was obtained via the UKCP consortium and the EPSRC grant ref EP/P022561/1, and the Cambridge Service for Data Driven Discovery (CSD3). T.B. acknowledges financial support from the Swiss National Science Foundation through the Early Postdoc Mobility Fellowship (grant number P2ELP2-199757). B.H. acknowledges support by the USA-Israel Binational Sci-

ence Foundation (grant No. 2020083) and the Israel Science Foundation (grants No. 1037/22 and 1312/22). Y.F. was supported by Schmidt Science Fellows, in partnership with the Rhodes Trust. T.E.L. is supported by start-up funds from the University of Delaware Department of Physics and Astronomy. M.R. and E.S. acknowledge computer time from the Max Planck Computing and Data Facility (MPCDF), funding from the IMPRS-UFAST program and the Lise-Meitner Excellence program. M.R. thanks Jan Berges for a careful read of section V C. M.C., M.K. and D.T. acknowledge funding from the Swiss National Science Foundation (SNSF) under the projects CRSII5.202296 and 200020.214879. M.C. and D.T. also acknowledge the support from the MARVEL National Centre of Competence in Research (NCCR) M.C. acknowledges funding from the European Research Council (ERC) under the European Union's Horizon 2020 research and innovation programme Grant No. 101001890-FIAMMA.

VII. DATA AVAILABILITY

The version of i-PI used in the examples and benchmarks can be obtained from <https://github.com/i-pi/>, using the tag `v3.0.0-alpha2`. The data required to reproduce the figures and the benchmark simulations are available at https://github.com/i-pi/ipiv3_data.

-
- [1] O. A. von Lilienfeld and K. Burke, Retrospective on a decade of machine learning for chemical discovery, *Nature Communications* **11**, 4895 (2020).
- [2] K. T. Butler, D. W. Davies, H. Cartwright, O. Isayev, and A. Walsh, Machine learning for molecular and materials science, *Nature* **559**, 547 (2018).
- [3] H. J. Kulik, T. Hammerschmidt, J. Schmidt, S. Botti, M. A. L. Marques, M. Boley, M. Scheffler, M. Todorović, P. Rinke, C. Oses, A. Smolyanyuk, S. Curtarolo, A. Tkatchenko, A. P. Bartók, S. Manzhos, M. Ihara, T. Carrington, J. Behler, O. Isayev, M. Veit, A. Grisafi, J. Nigam, M. Ceriotti, K. T. Schütt, J. Westermayr, M. Gastegger, R. J. Maurer, B. Kalita, K. Burke, R. Nagai, R. Akashi, O. Sugino, J. Hermann, F. Noé, S. Pilati, C. Draxl, M. Kuban, S. Rigamonti, M. Scheidgen, M. Esters, D. Hicks, C. Toher, P. V. Balachandran, I. Tamblyn, S. Whitelam, C. Bellinger, and L. M. Ghiringhelli, Roadmap on machine learning in electronic structure, *Electronic Structure* **4**, 023004 (2022).
- [4] V. L. Deringer, M. A. Caro, and G. Csányi, Machine learning interatomic potentials as emerging tools for materials science, *Advanced Materials* **31**, 1902765 (2019).
- [5] A. P. Bartók, S. De, C. Poelking, N. Bernstein, J. R. Kermode, G. Csányi, and M. Ceriotti, Machine learning unifies the modeling of materials and molecules, *Science Advances* **3**, e1701816 (2017).
- [6] Q. Tao, P. Xu, M. Li, and W. Lu, Machine learning for perovskite materials design and discovery, *npj Computational Materials* **7**, 23 (2021).
- [7] D. Lu, H. Wang, M. Chen, L. Lin, R. Car, W. E. W. Jia, and L. Zhang, 86 pflops deep potential molecular dynamics simulation of 100 million atoms with ab initio accuracy, *Computer Physics Communications* **259**, 107624 (2021).
- [8] J. Behler, First principles neural network potentials for reactive simulations of large molecular and condensed systems, *Angewandte Chemie International Edition* **56**, 12828 (2017).
- [9] I. Batatia, P. Benner, Y. Chiang, A. M. Elena, D. P. Kovács, J. Riebesell, X. R. Advincula, M. Asta, M. Avaylon, W. J. Baldwin, F. Berger, N. Bernstein, A. Bhowmik, S. M. Blau, V. Carare, J. P. Darby, S. De, F. D. Pia, V. L. Deringer, R. Elijošius, Z. El-Machachi, F. Falcioni, E. Fako, A. C. Ferrari, A. Genreith-Schriever, J. George, R. E. A. Goodall, C. P. Grey, P. Grigorev, S. Han, W. Handley, H. H. Heenen, K. Hermansson, C. Holm, J. Jaafar, S. Hofmann, K. S. Jakob, H. Jung, V. Kapil, A. D. Kaplan, N. Karimitari, J. R. Kermode, N. Kroupa, J. Kullgren, M. C. Kuner, D. Kuryla, G. Liepuoniute, J. T. Margraf, I.-B. Magdäu, A. Michaelides, J. H. Moore, A. A. Naik, S. P. Niblett, S. W. Norwood, N. O'Neill, C. Ortner, K. A. Persson, K. Reuter, A. S. Rosen, L. L. Schaaf, C. Schran, B. X.

- Shi, E. Sivonxay, T. K. Stenczel, V. Svahn, C. Sutton, T. D. Swinburne, J. Tilly, C. van der Oord, E. Varga-Umbrich, T. Vegge, M. Vondrák, Y. Wang, W. C. Witt, F. Zills, and G. Csányi, A foundation model for atomistic materials chemistry (2024), [arXiv:2401.00096](https://arxiv.org/abs/2401.00096).
- [10] O. T. Unke, S. Chmiela, H. E. Sauceda, M. Gastegger, I. Poltavsky, K. T. Schütt, A. Tkatchenko, and K.-R. Müller, Machine learning force fields, *Chemical Reviews* **121**, 10142 (2021).
- [11] A. Bruix, J. T. Margraf, M. Andersen, and K. Reuter, First-principles-based multiscale modelling of heterogeneous catalysis, *Nature Catalysis* **2**, 659 (2019).
- [12] P. Schlexer-Lamoureux, K. T. Winther, J. A. Garrido-Torres, V. Streibel, M. Zhao, M. Bajdich, F. Abild-Pedersen, and T. Bligaard, Machine learning for computational heterogeneous catalysis, *ChemCatChem* **11**, 3581 (2019).
- [13] S. Ma and Z.-P. Liu, Machine learning for atomic simulation and activity prediction in heterogeneous catalysis: Current status and future, *ACS Catalysis* **10**, 13213 (2020).
- [14] B. Cheng, E. A. Engel, J. Behler, C. Dellago, and M. Ceriotti, Ab initio thermodynamics of liquid and solid water, *Proceedings of the National Academy of Sciences* **116**, 1110 (2019).
- [15] V. L. Deringer and G. Csányi, Machine learning based interatomic potential for amorphous carbon, *Physical Review B* **95**, 094203 (2017).
- [16] S. Wengert, G. Csányi, K. Reuter, and J. T. Margraf, A hybrid machine learning approach for structure stability prediction in molecular co-crystal screenings, *Journal of Chemical Theory and Computation* **18**, 4586 (2022).
- [17] M. Ceriotti, J. More, and D. E. Manolopoulos, i-pi: A python interface for ab initio path integral molecular dynamics simulations, *Computer Physics Communications* **185**, 1019 (2014).
- [18] V. Kapil, M. Rossi, O. Marsalek, R. Petraglia, Y. Litman, T. Spura, B. Cheng, A. Cuzzocrea, R. H. Meißner, D. M. Wilkins, B. A. Helfrecht, P. Juda, S. P. Bivenvenue, W. Fang, J. Kessler, I. Poltavsky, S. Vandenbrande, J. Wieme, C. Corminboeuf, T. D. Kühne, D. E. Manolopoulos, T. E. Markland, J. O. Richardson, A. Tkatchenko, G. A. Tribello, V. Van Speybroeck, and M. Ceriotti, i-pi 2.0: A universal force engine for advanced molecular simulations, *Computer Physics Communications* **236**, 214 (2019).
- [19] A. Schobert, J. Berges, E. G. C. P. van Loon, M. A. Sentef, S. Brener, M. Rossi, and T. O. Wehling, Ab initio electron-lattice downfolding: Potential energy landscapes, anharmonicity, and molecular dynamics in charge density wave materials, *SciPost Phys.* **16**, 046 (2024), [arXiv:2303.07261](https://arxiv.org/abs/2303.07261).
- [20] M. Jacobs, K. Fidanyan, M. Rossi, and C. Cocchi, Impact of nuclear effects on the ultrafast dynamics of an organic/inorganic mixed-dimensional interface, *Electronic Structure* (2024).
- [21] J. Lan, V. V. Rybkin, and A. Pasquarello, Temperature dependent properties of the aqueous electron, *Angewandte Chemie International Edition* **61**, e202209398 (2022).
- [22] B. Cheng, G. Mazzola, C. J. Pickard, and M. Ceriotti, Evidence for supercritical behaviour of high-pressure liquid hydrogen, *Nature* **585**, 217 (2020).
- [23] V. Kapil, C. Schran, A. Zen, J. Chen, C. J. Pickard, and A. Michaelides, The first-principles phase diagram of monolayer nanoconfined water, *Nature* **609**, 512 (2022).
- [24] Y. Litman, K.-Y. Chiang, T. Seki, Y. Nagata, and M. Bonn, Surface stratification determines the interfacial water structure of simple electrolyte solutions, *Nature Chemistry* **16**, 644 (2024).
- [25] Y. Litman, J. Lan, Y. Nagata, and D. M. Wilkins, Fully first-principles surface spectroscopy with machine learning, *The Journal of Physical Chemistry Letters* **14**, 8175 (2023).
- [26] K. Inoue, Y. Litman, D. M. Wilkins, Y. Nagata, and M. Okuno, Is unified understanding of vibrational coupling of water possible? hyper-raman measurement and machine learning spectra, *The Journal of Physical Chemistry Letters* **14**, 3063 (2023).
- [27] K. Fidanyan, G. Liu, and M. Rossi, Ab initio study of water dissociation on a charged Pd(111) surface, *The Journal of Chemical Physics* **158**, 094707 (2023), 2212.08855.
- [28] J. J. Mortensen, GPAW: An open Python package for electronic structure calculations, *The Journal of Chemical Physics* **160**, 092503 (2024).
- [29] Q. Sun, X. Zhang, S. Banerjee, P. Bao, M. Barbry, N. S. Blunt, N. A. Bogdanov, G. H. Booth, J. Chen, Z.-H. Cui, J. J. Eriksen, Y. Gao, S. Guo, J. Hermann, M. R. Hermes, K. Koh, P. Koval, S. Lehtola, Z. Li, J. Liu, N. Mardirossian, J. D. McClain, M. Motta, B. Mussard, H. Q. Pham, A. Pulkin, W. Purwanto, P. J. Robinson, E. Ronca, E. R. Sayfutyarova, M. Scheurer, H. F. Schurkus, J. E. T. Smith, C. Sun, S.-N. Sun, S. Upadhyay, L. K. Wagner, X. Wang, A. White, J. D. Whitfield, M. J. Williamson, S. Wouters, J. Yang, J. M. Yu, T. Zhu, T. C. Berkelbach, S. Sharma, A. Y. Sokolov, and G. K.-L. Chan, Recent developments in the PySCF program package, *The Journal of Chemical Physics* **153**, 024109 (2020).
- [30] T. E. Markland and D. E. Manolopoulos, An efficient ring polymer contraction scheme for imaginary time path integral simulations, *The Journal of Chemical Physics* **129**, 024105 (2008).
- [31] T. E. Markland and D. E. Manolopoulos, A refined ring polymer contraction scheme for systems with electrostatic interactions, *Chem. Phys. Lett.* **464**, 256 (2008).
- [32] L. Gigli, D. Tisi, F. Grasselli, and M. Ceriotti, Mechanism of charge transport in lithium thiophosphate, *Chemistry of Materials* **36**, 1482 (2024).
- [33] D. Tisi, F. Grasselli, L. Gigli, and M. Ceriotti, Thermal transport of Li_3PS_4 solid electrolytes with ab initio accuracy (2024), [arXiv:2401.12936](https://arxiv.org/abs/2401.12936).
- [34] V. Kapil, J. VandeVondele, and M. Ceriotti, Accurate molecular dynamics and nuclear quantum effects at low cost by multiple steps in real and imaginary time: Using density functional theory to accelerate wavefunction methods, *The Journal of Chemical Physics* **144**, 054111 (2016).
- [35] Y. Litman, D. Donadio, M. Ceriotti, and M. Rossi, Decisive role of nuclear quantum effects on surface mediated water dissociation at finite temperature, *The Journal of Chemical Physics* **148**, 102320 (2018).
- [36] A. H. Larsen, J. J. Mortensen, J. Blomqvist, I. E. Castelli, R. Christensen, M. Dułak, J. Friis, M. N. Groves, B. Hammer, C. Hargus, E. D. Hermes, P. C. Jennings, P. B. Jensen, J. Kermode, J. R. Kitchin, E. L.

- Kolsbjerg, J. Kubal, K. Kaasbjerg, S. Lysgaard, J. B. Maronsson, T. Maxson, T. Olsen, L. Pastewka, A. Peterson, C. Rostgaard, J. Schiøtz, O. Schütt, M. Strange, K. S. Thygesen, T. Vegge, L. Vilhelmsen, M. Walter, Z. Zeng, and K. W. Jacobsen, The atomic simulation environment—a python library for working with atoms, *Journal of Physics: Condensed Matter* **29**, 273002 (2017).
- [37] A. P. Thompson, H. M. Aktulga, R. Berger, D. S. Bolinteanu, W. M. Brown, P. S. Crozier, P. J. in 't Veld, A. Kohlmeyer, S. G. Moore, T. D. Nguyen, R. Shan, M. J. Stevens, J. Tranchida, C. Trott, and S. J. Plimpton, LAMMPS - a flexible simulation tool for particle-based materials modeling at the atomic, meso, and continuum scales, *Computer Physics Communications* **271**, 108171 (2022).
- [38] S. J. Clark, M. D. Segall, C. J. Pickard, P. J. Hasnip, M. I. J. Probert, K. Refson, and M. C. Payne, First principles methods using castep, *Zeitschrift für Kristallographie - Crystalline Materials* **220**, 567 (2005).
- [39] T. D. Kühne, M. Iannuzzi, M. Del Ben, V. V. Rybkin, P. Seewald, F. Stein, T. Laino, R. Z. Khatullin, O. Schütt, F. Schiffmann, D. Golze, J. Wilhelm, S. Chulkov, M. H. Bani-Hashemian, V. Weber, U. Borstnik, M. Tailliefumier, A. S. Jakobovits, A. Lazaro, H. Pabst, T. Müller, R. Schade, M. Guidon, S. Andermatt, N. Holmberg, G. K. Schenter, A. Hehn, A. Bussy, F. Belleflamme, G. Tabacchi, A. Glöb, M. Lass, I. Bethune, C. J. Mundy, C. Plessl, M. Watkins, J. VandeVondele, M. Krack, and J. Hutter, CP2K: An electronic structure and molecular dynamics software package - Quickstep: Efficient and accurate electronic structure calculations, *The Journal of Chemical Physics* **152**, 194103 (2020).
- [40] B. Hourahine, B. Aradi, V. Blum, F. Bonafé, A. Buccheri, C. Camacho, C. Cevallos, M. Y. Deshayé, T. Dumitrică, A. Dominguez, S. Ehlert, M. Elstner, T. van der Heide, J. Hermann, S. Irle, J. J. Kranz, C. Köhler, T. Kowalczyk, T. Kubař, I. S. Lee, V. Lutsker, R. J. Maurer, S. K. Min, I. Mitchell, C. Negre, T. A. Niehaus, A. M. N. Niklasson, A. J. Page, A. Pecchia, G. Penazzi, M. P. Persson, J. Řezáč, C. G. Sánchez, M. Sternberg, M. Stöhr, F. Stuckenberg, A. Tkatchenko, V. W.-z. Yu, and T. Frauenheim, DFTB+, a software package for efficient approximate density functional theory based atomistic simulations, *The Journal of Chemical Physics* **152**, 124101 (2020).
- [41] S. Chmiela, H. E. Sauceda, I. Poltavsky, K.-R. Müller, and A. Tkatchenko, sgdml: Constructing accurate and data efficient molecular force fields using machine learning, *Computer Physics Communications* **240**, 38 (2019).
- [42] V. Blum, R. Gehrke, F. Hanke, P. Havu, V. Havu, X. Ren, K. Reuter, and M. Scheffler, Ab initio molecular simulations with numeric atom-centered orbitals, *Computer Physics Communications* **180**, 2175 (2009).
- [43] F. Musil, M. Stricker, A. Goscinski, F. Giberti, M. Veit, T. Junge, G. Fraux, M. Ceriotti, R. Cersovsky, M. Willatt, and A. Grisafi, cosmo-epfl/librascal, zenodo. <https://doi.org/10.5281/zenodo.4526063> (2021).
- [44] P. Giannozzi, S. Baroni, N. Bonini, M. Calandra, R. Car, C. Cavazzoni, D. Ceresoli, G. L. Chiarotti, M. Cococcioni, I. Dabo, A. D. Corso, S. de Gironcoli, S. Fabris, G. Fratesi, R. Gebauer, U. Gerstmann, C. Gougoussis, A. Kokalj, M. Lazzeri, L. Martin-Samos, N. Marzari, F. Mauri, R. Mazzarello, S. Paolini, A. Pasquarello, L. Paulatto, C. Sbraccia, S. Scandolo, G. Sclauzero, A. P. Seitsonen, A. Smogunov, P. Umari, and R. M. Wentzcovitch, Quantum espresso: a modular and open-source software project for quantum simulations of materials, *Journal of Physics: Condensed Matter* **21**, 395502 (2009).
- [45] P. Giannozzi, O. Andreussi, T. Brumme, O. Bunau, M. B. Nardelli, M. Calandra, R. Car, C. Cavazzoni, D. Ceresoli, M. Cococcioni, N. Colonna, I. Carnimeo, A. D. Corso, S. de Gironcoli, P. Delugas, R. A. D. Jr, A. Ferretti, A. Floris, G. Fratesi, G. Fugallo, R. Gebauer, U. Gerstmann, F. Giustino, T. Gorni, J. Jia, M. Kawamura, H.-Y. Ko, A. Kokalj, E. Küçükbenli, M. Lazzeri, M. Marsili, N. Marzari, F. Mauri, N. L. Nguyen, H.-V. Nguyen, A. O. de-la Roza, L. Paulatto, S. Poncé, D. Rocca, R. Sabatini, B. Santra, M. Schlipf, A. P. Seitsonen, A. Smogunov, I. Timrov, T. Thonhauser, P. Umari, N. Vast, X. Wu, and S. Baroni, Advanced capabilities for materials modelling with quantum espresso, *Journal of Physics: Condensed Matter* **29**, 465901 (2017).
- [46] P. Giannozzi, O. Baseggio, P. Bonfà, D. Brunato, R. Car, I. Carnimeo, C. Cavazzoni, S. de Gironcoli, P. Delugas, F. Ferrari Ruffino, A. Ferretti, N. Marzari, I. Timrov, A. Urru, and S. Baroni, Quantum espresso toward the exascale, *The Journal of Chemical Physics* **152**, 154105 (2020).
- [47] G. Kresse and J. Furthmüller, Efficient iterative schemes for ab initio total-energy calculations using a plane-wave basis set, *Physical Review B* **54**, 11169 (1996).
- [48] J. Berges, A. Schobert, E. G. C. P. van Loon, M. Rösner, and T. O. Wehling, elphmod: Python modules for electron-phonon models, Zenodo (2017), doi:10.5281/zenodo.5919991.
- [49] S. V. T. Verstraelen, L. Vanduyfhuys and S. M. J. Rogge, Yaff, yet another force field, <https://molmod.ugent.be/software/>.
- [50] G. Bussi, D. Donadio, and M. Parrinello, Canonical sampling through velocity rescaling, *The Journal of Chemical Physics* **126**, 14101 (2007).
- [51] M. Ceriotti, M. Parrinello, T. E. Markland, and D. E. Manolopoulos, Efficient stochastic thermostating of path integral molecular dynamics., *The Journal of Chemical Physics* **133**, 124104 (2010).
- [52] M. Ceriotti, G. Bussi, and M. Parrinello, Langevin Equation with Colored Noise for Constant-Temperature Molecular Dynamics Simulations, *Physical Review Letters* **102**, 020601 (2009).
- [53] M. Ceriotti, G. Bussi, and M. Parrinello, Colored-Noise Thermostats à la Carte, *Journal of Chemical Theory and Computation* **6**, 1170 (2010).
- [54] M. Ceriotti, G. Bussi, and M. Parrinello, Nuclear Quantum Effects in Solids Using a Colored-Noise Thermostat, *Physical Review Letters* **103**, 30603 (2009).
- [55] M. Ceriotti and M. Parrinello, The δ -thermostat: selective normal-modes excitation by colored-noise Langevin dynamics, *Procedia Computer Science* **1**, 1607 (2010).
- [56] R. Dettori, M. Ceriotti, J. Hunger, C. Melis, L. Colombo, and D. Donadio, Simulating Energy Relaxation in Pump-Probe Vibrational Spectroscopy of Hydrogen-Bonded Liquids, *Journal of Chemical Theory and Computation* **13**, 1284 (2017).

- [57] M. Ceriotti and D. E. Manolopoulos, Efficient First-Principles Calculation of the Quantum Kinetic Energy and Momentum Distribution of Nuclei, *Physical Review Letters* **109**, 100604 (2012).
- [58] M. Rossi, V. Kapil, and M. Ceriotti, Fine tuning classical and quantum molecular dynamics using a generalized Langevin equation, *The Journal of Chemical Physics* **148**, 102301 (2018).
- [59] M. Hijazi, D. M. D. Wilkins, and M. Ceriotti, Fast-forward Langevin dynamics with momentum flips, *The Journal of Chemical Physics* **148**, 184109 (2018).
- [60] F. R. Krajewski and M. Parrinello, Linear scaling electronic structure calculations and accurate statistical mechanics sampling with noisy forces, *Physical Review B* **73**, 041105 (2006).
- [61] T. D. Kühne, M. Krack, F. R. Mohamed, and M. Parrinello, Efficient and accurate car-parrinello-like approach to born-oppenheimer molecular dynamics, *Physical Review Letters* **98**, 066401 (2007).
- [62] G. Bussi, T. Zykova-Timan, and M. Parrinello, Isothermal-isobaric molecular dynamics using stochastic velocity rescaling, *The Journal of Chemical Physics* **130**, 074101 (2009).
- [63] P. Raiteri, J. D. Gale, and G. Bussi, Reactive force field simulation of proton diffusion in bazo3 using an empirical valence bond approach, *Journal of Physics: Condensed Matter* **23**, 334213 (2011).
- [64] G. J. Martyna, A. Hughes, and M. E. Tuckerman, Molecular dynamics algorithms for path integrals at constant pressure, *The Journal of Chemical Physics* **110**, 3275 (1999).
- [65] V. Kapil, J. Wieme, S. Vandenbrande, A. Lemaire, V. Van Speybroeck, and M. Ceriotti, Modeling the structural and thermal properties of loaded metal-organic frameworks. an interplay of quantum and anharmonic fluctuations, *Journal of Chemical Theory and Computation* **15**, 3237 (2019).
- [66] G. Henkelman, B. P. Uberuaga, and H. Jónsson, A climbing image nudged elastic band method for finding saddle points and minimum energy paths, *The Journal of Chemical Physics* **113**, 9901 (2000).
- [67] G. Henkelman and H. Jónsson, Improved tangent estimate in the nudged elastic band method for finding minimum energy paths and saddle points, *The Journal of Chemical Physics* **113**, 9978 (2000).
- [68] J. Nichols, H. Taylor, P. Schmidt, and J. Simons, Walking on potential energy surfaces, *The Journal of Chemical Physics* **92**, 340 (1990).
- [69] V. Kapil, E. Engel, M. Rossi, and M. Ceriotti, Assessment of approximate methods for anharmonic free energies, *Journal of Chemical Theory and Computation* **15**, 5845 (2019).
- [70] M. Rossi, P. Gasparotto, and M. Ceriotti, Anharmonic and Quantum Fluctuations in Molecular Crystals: A First-Principles Study of the Stability of Paracetamol, *Physical Review Letters* **117**, 115702 (2016).
- [71] R. Petraglia, A. Nicolai, M. M. D. Wodrich, M. Ceriotti, and C. Corminboeuf, Beyond static structures: Putting forth REMD as a tool to solve problems in computational organic chemistry, *Journal of Computational Chemistry* **37**, 83 (2016).
- [72] J. Liu, R. S. Andino, C. M. Miller, X. Chen, D. M. Wilkins, M. Ceriotti, and D. E. Manolopoulos, A Surface-Specific Isotope Effect in Mixtures of Light and Heavy Water, *The Journal of Physical Chemistry C* **117**, 2944 (2013).
- [73] B. Cheng, J. Behler, and M. Ceriotti, Nuclear Quantum Effects in Water at the Triple Point: Using Theory as a Link Between Experiments, *The Journal of Physical Chemistry Letters* **7**, 2210 (2016).
- [74] I. R. Craig and D. E. Manolopoulos, Quantum statistics and classical mechanics: Real time correlation functions from ring polymer molecular dynamics, *The Journal of Chemical Physics* **121**, 3368 (2004).
- [75] S. Habershon, D. E. Manolopoulos, T. E. Markland, and T. F. Miller, Ring-polymer molecular dynamics: quantum effects in chemical dynamics from classical trajectories in an extended phase space., *Annual review of physical chemistry* **64**, 387 (2013).
- [76] J. Cao and G. A. Voth, A new perspective on quantum time correlation functions, *The Journal of Chemical Physics* **99**, 10070 (1993).
- [77] J. Cao and G. A. Voth, The formulation of quantum statistical mechanics based on the Feynman path centroid density. IV. Algorithms for centroid molecular dynamics, *The Journal of Chemical Physics* **101**, 6168 (1994).
- [78] M. Rossi, M. Ceriotti, and D. E. Manolopoulos, How to remove the spurious resonances from ring polymer molecular dynamics., *The Journal of Chemical Physics* **140**, 234116 (2014).
- [79] F. Musil, I. Zaporozhets, F. Noé, C. Clementi, and V. Kapil, Quantum dynamics using path integral coarse-graining, *The Journal of Chemical Physics* **10.1063/5.0120386** (2022).
- [80] Y. Litman, J. O. Richardson, T. Kumagai, and M. Rossi, Elucidating the nuclear quantum dynamics of intramolecular double hydrogen transfer in porphycene, *Journal of the American Chemical Society* **141**, 2526 (2019).
- [81] V. Kapil, J. Behler, and M. Ceriotti, High order path integrals made easy, *The Journal of Chemical Physics* **145**, 234103 (2016).
- [82] I. Poltavsky and A. Tkatchenko, Modeling quantum nuclei with perturbed path integral molecular dynamics, *Chemical Science* **7**, 1368 (2016).
- [83] V. Kapil, A. Cuzzocrea, and M. Ceriotti, Anisotropy of the Proton Momentum Distribution in Water, *The Journal of Physical Chemistry B* **122**, 6048 (2018).
- [84] T. M. Yamamoto, Path-integral virial estimator based on the scaling of fluctuation coordinates: Application to quantum clusters with fourth-order propagators, *The Journal of Chemical Physics* **123**, 104101 (2005).
- [85] M. Ceriotti and T. E. Markland, Efficient methods and practical guidelines for simulating isotope effects., *The Journal of Chemical Physics* **138**, 014112 (2013).
- [86] L. Lin, J. A. Morrone, R. Car, and M. Parrinello, Displaced Path Integral Formulation for the Momentum Distribution of Quantum Particles, *Physical Review Letters* **105**, 110602 (2010).
- [87] M. Ceriotti, G. A. R. Brain, O. Riordan, and D. E. Manolopoulos, The inefficiency of re-weighted sampling and the curse of system size in high order path integration, *Proceedings of the Royal Society A: Mathematical, Physical and Engineering Sciences* **468**, 2 (2011).
- [88] S. S. Jang and G. A. Voth, Applications of higher order composite factorization schemes in imaginary time path integral simulations, *The Journal of Chemical Physics* **115**, 7832 (2001).

- [89] B. Hirshberg, V. Rizzi, and M. Parrinello, Path integral molecular dynamics for bosons, *Proceedings of the National Academy of Sciences* **116**, 21445 (2019).
- [90] Y. M. Y. Feldman and B. Hirshberg, Quadratic scaling bosonic path integral molecular dynamics, *The Journal of Chemical Physics* **159**, 154107 (2023).
- [91] B. Hirshberg, M. Invernizzi, and M. Parrinello, Path integral molecular dynamics for fermions: Alleviating the sign problem with the Bogoliubov inequality, *The Journal of Chemical Physics* **152**, 171102 (2020).
- [92] T. E. Li, J. E. Subotnik, and A. Nitzan, Cavity Molecular Dynamics Simulations of Liquid Water under Vibrational Ultrastrong Coupling, *Proc. Natl. Acad. Sci.* **117**, 18324 (2020).
- [93] T. E. Li, A. Nitzan, S. Hammes-Schiffer, and J. E. Subotnik, Quantum Simulations of Vibrational Strong Coupling via Path Integrals, *The Journal of Physical Chemistry Letters* **13**, 3890 (2022).
- [94] T. Hasegawa and Y. Tanimura, Calculating fifth-order Raman signals for various molecular liquids by equilibrium and nonequilibrium hybrid molecular dynamics simulation algorithms, *The Journal of Chemical Physics* **125**, 074512 (2006).
- [95] T. Begušić, X. Tao, G. A. Blake, and I. Miller, Thomas F., Equilibrium–nonequilibrium ring-polymer molecular dynamics for nonlinear spectroscopy, *The Journal of Chemical Physics* **156**, 131102 (2022).
- [96] T. Begušić and G. A. Blake, Two-dimensional infrared-raman spectroscopy as a probe of water’s tetrahedrality, *Nature Communications* **14**, 1950 (2023).
- [97] Y. Litman, E. S. Pócs, C. L. Box, R. Martinazzo, R. J. Maurer, and M. Rossi, Dissipative tunneling rates through the incorporation of first-principles electronic friction in instanton rate theory. I. Theory, *The Journal of Chemical Physics* **156**, 194106 (2022).
- [98] Y. Litman, E. S. Pócs, C. L. Box, R. Martinazzo, R. J. Maurer, and M. Rossi, Dissipative tunneling rates through the incorporation of first-principles electronic friction in instanton rate theory. II. Benchmarks and applications, *The Journal of Chemical Physics* **156**, 194107 (2022).
- [99] G. Imbalzano, Y. Zhuang, V. Kapil, K. Rossi, E. A. Engel, F. Grasselli, and M. Ceriotti, Uncertainty estimation for molecular dynamics and sampling, *The Journal of Chemical Physics* **154**, 074102 (2021).
- [100] M. Kellner and M. Ceriotti, Uncertainty quantification by direct propagation of shallow ensembles (2024), [arXiv:2402.16621](https://arxiv.org/abs/2402.16621).
- [101] G. Bussi, D. Donadio, and M. Parrinello, Canonical sampling through velocity rescaling, *The Journal of Chemical Physics* **126**, 014101 (2007).
- [102] M. Suzuki, Hybrid exponential product formulas for unbounded operators with possible applications to Monte Carlo simulations, *Physics Letters A* **201**, 425 (1995).
- [103] B. Leimkuhler and C. Matthews, Robust and efficient configurational molecular sampling via Langevin dynamics, *The Journal of Chemical Physics* **138** (2013).
- [104] J. Nagle, Congestion control in ip/tcp internetworks, *SIGCOMM Comput. Commun. Rev.* **14**, 11–17 (1984).
- [105] J. Han, L. Zhang, R. Car, and W. E, Deep potential: A general representation of a many-body potential energy surface, *Communications in Computational Physics* **23**, 629 (2018).
- [106] H. Wang, L. Zhang, J. Han, and W. E, Deepmd-kit: A deep learning package for many-body potential energy representation and molecular dynamics, *Computer Physics Communications* **228**, 178 (2018).
- [107] J. Zeng, D. Zhang, D. Lu, P. Mo, Z. Li, Y. Chen, M. Rynik, L. Huang, Z. Li, S. Shi, Y. Wang, H. Ye, P. Tuo, J. Yang, Y. Ding, Y. Li, D. Tisi, Q. Zeng, H. Bao, Y. Xia, J. Huang, K. Muraoka, Y. Wang, J. Chang, F. Yuan, S. L. Bore, C. Cai, Y. Lin, B. Wang, J. Xu, J.-X. Zhu, C. Luo, Y. Zhang, R. E. A. Goodall, W. Liang, A. K. Singh, S. Yao, J. Zhang, R. Wentzcovitch, J. Han, J. Liu, W. Jia, D. M. York, W. E, R. Car, L. Zhang, and H. Wang, DeePMD-kit v2: A software package for deep potential models, *The Journal of Chemical Physics* **159**, 054801 (2023).
- [108] P. Ravindra, X. R. Advincula, C. Schran, A. Michaelides, and V. Kapil, A quasi-one-dimensional hydrogen-bonded monolayer ice phase (2023), [arXiv:2312.01340](https://arxiv.org/abs/2312.01340) [cond-mat].
- [109] D. M. Ceperley, Path integrals in the theory of condensed helium, *Reviews of Modern Physics* **67**, 279 (1995).
- [110] C. W. Myung, B. Hirshberg, and M. Parrinello, Prediction of a supersolid phase in high-pressure deuterium, *Physical Review Letters* **128**, 045301 (2022).
- [111] T. Dornheim, M. Invernizzi, J. Vorberger, and B. Hirshberg, Attenuating the fermion sign problem in path integral Monte Carlo simulations using the Bogoliubov inequality and thermodynamic integration, *The Journal of Chemical Physics* **153**, 234104 (2020).
- [112] T. Dornheim, P. Tolias, S. Groth, Z. A. Moldabekov, J. Vorberger, and B. Hirshberg, Fermionic physics from ab initio path integral Monte Carlo simulations of fictitious identical particles, *The Journal of Chemical Physics* **159**, 164113 (2023).
- [113] M. Head-Gordon and J. C. Tully, Molecular dynamics with electronic frictions, *The Journal of Chemical Physics* **103**, 10137 (1995).
- [114] W. Dou, G. Miao, and J. E. Subotnik, Born-oppenheimer dynamics, electronic friction, and the inclusion of electron-electron interactions, *Physical Review Letters* **119**, 046001 (2017).
- [115] W. Dou and J. E. Subotnik, Perspective: How to understand electronic friction, *The Journal of Chemical Physics* **148**, 230901 (2018).
- [116] R. Martinazzo and I. Burghardt, Quantum theory of electronic friction, *Physical Review A* **105**, 052215 (2022).
- [117] R. Martinazzo and I. Burghardt, Quantum dynamics with electronic friction, *Physical Review Letters* **128**, 206002 (2022).
- [118] R. Martinazzo and I. Burghardt, Quantum hydrodynamics of coupled electron-nuclear systems (2023), [arXiv:2310.08766](https://arxiv.org/abs/2310.08766).
- [119] R. J. Maurer, M. Askerka, V. S. Batista, and J. C. Tully, Ab initio tensorial electronic friction for molecules on metal surfaces: Nonadiabatic vibrational relaxation, *Physical Review B* **94**, 115432 (2016).
- [120] J. O. Richardson, Ring-polymer instanton theory, *International Reviews in Physical Chemistry* **37**, 171 (2018).
- [121] Y. Litman and M. Rossi, Multidimensional hydrogen tunneling in supported molecular switches: The role of surface interactions, *Physical Review Letters* **125**, 216001 (2020).

- [122] C. L. Box, W. G. Stark, and R. J. Maurer, Ab initio calculation of electron-phonon linewidths and molecular dynamics with electronic friction at metal surfaces with numeric atom-centred orbitals, *Electronic Structure* **5**, 035005 (2023).
- [123] J. O. Richardson and S. C. Althorpe, Ring-polymer molecular dynamics rate-theory in the deep-tunneling regime: Connection with semiclassical instanton theory, *The Journal of Chemical Physics* **131**, 214106 (2009).
- [124] A. N. Beyer, J. O. Richardson, P. J. Knowles, J. Rommel, and S. C. Althorpe, Quantum tunneling rates of gas-phase reactions from on-the-fly instanton calculations, *The Journal of Physical Chemistry Letters* **7**, 4374 (2016).
- [125] Y. Litman, *Tunneling and Zero-Point Energy Effects in Multidimensional Hydrogen Transfer Reactions: From Gas Phase to Adsorption on Metal Surfaces*, Ph.D. thesis, Freie Universität Berlin (2020).
- [126] P. Salén, M. Basini, S. Bonetti, J. Hebling, M. Krasilnikov, A. Y. Nikitin, G. Shamuilov, Z. Tibai, V. Zhaunerchyk, and V. Goryashko, Matter manipulation with extreme terahertz light: Progress in the enabling thz technology, *Physics Reports* **836-837**, 1 (2019).
- [127] A. de la Torre, D. M. Kennes, M. Claassen, S. Gerber, J. W. McIver, and M. A. Sentef, Colloquium: Nonthermal pathways to ultrafast control in quantum materials, *Reviews of Modern Physics* **93**, 041002 (2021).
- [128] A. S. Disa, T. F. Nova, and A. Cavalleri, Engineering crystal structures with light, *Nature Physics* **17**, 1087 (2021).
- [129] D. M. Juraschek, M. Fechner, and N. A. Spaldin, Ultrafast structure switching through nonlinear phononics, *Physical Review Letters* **118**, 054101 (2017).
- [130] A. Subedi, A. Cavalleri, and A. Georges, Theory of nonlinear phononics for coherent light control of solids, *Physical Review B* **89**, 220301 (2014).
- [131] M. Först, C. Manzoni, S. Kaiser, Y. Tomioka, Y. Tokura, R. Merlin, and A. Cavalleri, Nonlinear phononics as an ultrafast route to lattice control, *Nature Physics* **7**, 854 (2011).
- [132] N. A. Spaldin, A beginner's guide to the modern theory of polarization, *Journal of Solid State Chemistry* **195**, 2 (2012), polar Inorganic Materials: Design Strategies and Functional Properties.
- [133] S. Baroni, S. de Gironcoli, A. Dal Corso, and P. Giannozzi, Phonons and related crystal properties from density-functional perturbation theory, *Reviews of Modern Physics* **73**, 515 (2001).
- [134] H. Shang, N. Raimbault, P. Rinke, M. Scheffler, M. Rossi, and C. Carbogno, All-electron, real-space perturbation theory for homogeneous electric fields: theory, implementation, and application within dft, *New Journal of Physics* **20**, 073040 (2018).
- [135] H. Partridge and D. W. Schwenke, The determination of an accurate isotope dependent potential energy surface for water from extensive ab initio calculations and experimental data, *The Journal of Chemical Physics* **106**, 4618 (1997).
- [136] F. Musil, M. J. Willatt, M. A. Langovoy, and M. Ceriotti, Fast and Accurate Uncertainty Estimation in Chemical Machine Learning, *Journal of Chemical Theory and Computation* **15**, 906 (2019).
- [137] B. Lakshminarayanan, A. Pritzel, and C. Blundell, Simple and scalable predictive uncertainty estimation using deep ensembles, in *Advances in Neural Information Processing Systems*, Vol. 30, edited by I. Guyon, U. V. Luxburg, S. Bengio, H. Wallach, R. Fergus, S. Vishwanathan, and R. Garnett (Curran Associates, Inc., 2017).
- [138] G. Kunapuli, *Ensemble Methods for Machine Learning* (Manning, 2023).
- [139] A. Ashukha, A. Lyzhov, D. Molchanov, and D. Vetrov, Pitfalls of in-domain uncertainty estimation and ensembling in deep learning (2021), [arXiv:2002.06470](https://arxiv.org/abs/2002.06470).
- [140] R. Rahaman and A. Thiery, Uncertainty quantification and deep ensembles, in *Advances in Neural Information Processing Systems*, Vol. 34, edited by M. Ranzato, A. Beygelzimer, Y. Dauphin, P. Liang, and J. W. Vaughan (Curran Associates, Inc., 2021) pp. 20063–20075.
- [141] F. Bigi, S. Chong, M. Ceriotti, and F. Grasselli, A prediction rigidity formalism for low-cost uncertainties in trained neural networks (2024), [arXiv:2403.02251](https://arxiv.org/abs/2403.02251).
- [142] G. Imbalzano, Y. Zhuang, V. Kapil, K. Rossi, E. A. Engel, F. Grasselli, and M. Ceriotti, Uncertainty estimation for molecular dynamics and sampling, *The Journal of Chemical Physics* **154**, 074102 (2021).
- [143] J. Behler and M. Parrinello, Generalized Neural-Network Representation of High-Dimensional Potential-Energy Surfaces, *Physical Review Letters* **98**, 146401 (2007).
- [144] A. P. Bartók, R. Kondor, and G. Csányi, On representing chemical environments, *Physical Review B* **87**, 184115 (2013).
- [145] U. R. Pedersen, F. Hummel, and C. Dellago, Computing the crystal growth rate by the interface pinning method., *The Journal of Chemical Physics* **142**, 44104 (2015).
- [146] M. Bonomi, D. Branduardi, G. Bussi, C. Camilloni, D. Provasi, P. Raiteri, D. Donadio, F. Marinelli, F. Pietrucci, R. A. Broglia, and M. Parrinello, PLUMED: A portable plugin for free-energy calculations with molecular dynamics, *Computer Physics Communications*. **180**, 1961 (2009).
- [147] G. M. Torrie and J. P. Valleau, Nonphysical sampling distributions in Monte Carlo free-energy estimation: Umbrella sampling, *Journal of Computational Physics* **23**, 187 (1977).
- [148] R. F. Ribeiro, L. A. Martínez-Martínez, M. Du, J. Campos-Gonzalez-Angulo, and J. Yuen-Zhou, Polariton Chemistry: Controlling Molecular Dynamics with Optical Cavities, *Chemical Science* **9**, 6325 (2018).
- [149] T. E. Li, B. Cui, J. E. Subotnik, and A. Nitzan, Molecular Polaritonics: Chemical Dynamics Under Strong Light–Matter Coupling, *Annu. Rev. Phys. Chem.* **73**, 43 (2022).
- [150] J. Fregoni, F. J. Garcia-Vidal, and J. Feist, Theoretical Challenges in Polaritonic Chemistry, *ACS Photonics* **9**, 1096 (2022).
- [151] A. Mandal, M. A. Taylor, B. M. Weight, E. R. Koessler, X. Li, and P. Huo, Theoretical Advances in Polariton Chemistry and Molecular Cavity Quantum Electrodynamics, *Chemical Reviews* **123**, 9786 (2023).
- [152] M. Ruggenthaler, D. Sidler, and A. Rubio, Understanding Polaritonic Chemistry from Ab Initio Quantum Electrodynamics, *Chemical Reviews* **123**, 11191 (2023).

- [153] A. Shalabney, J. George, J. Hutchison, G. Pupillo, C. Genet, and T. W. Ebbesen, Coherent Coupling of Molecular Resonators with a Microcavity Mode, *Nature Communications* **6**, 5981 (2015).
- [154] J. P. Long and B. S. Simpkins, Coherent Coupling between a Molecular Vibration and Fabry–Perot Optical Cavity to Give Hybridized States in the Strong Coupling Limit, *ACS Photonics* **2**, 130 (2015).
- [155] A. Thomas, J. George, A. Shalabney, M. Dryzhakov, S. J. Varma, J. Moran, T. Chervy, X. Zhong, E. Devaux, C. Genet, J. A. Hutchison, and T. W. Ebbesen, Ground-State Chemical Reactivity under Vibrational Coupling to the Vacuum Electromagnetic Field, *Angew. Chemie Int. Ed.* **55**, 11462 (2016).
- [156] A. Thomas, L. Lethuillier-Karl, K. Nagarajan, R. M. A. Vergauwe, J. George, T. Chervy, A. Shalabney, E. Devaux, C. Genet, J. Moran, and T. W. Ebbesen, Tilting a Ground-State Reactivity Landscape by Vibrational Strong Coupling, *Science* **363**, 615 (2019).
- [157] B. Xiang, R. F. Ribeiro, M. Du, L. Chen, Z. Yang, J. Wang, J. Yuen-Zhou, and W. Xiong, Intermolecular Vibrational Energy Transfer Enabled by Microcavity Strong Light–Matter Coupling, *Science* **368**, 665 (2020).
- [158] J. Flick, M. Ruggenthaler, H. Appel, and A. Rubio, Atoms and Molecules in Cavities, from Weak to Strong Coupling in Quantum-Electrodynamics (QED) Chemistry, *Proc. Natl. Acad. Sci.* **114**, 3026 (2017).
- [159] T. E. Li, A. Nitzan, and J. E. Subotnik, Cavity Molecular Dynamics Simulations of Vibrational Polariton-Enhanced Molecular Nonlinear Absorption, *The Journal of Chemical Physics* **154**, 094124 (2021).
- [160] T. E. Li, A. Nitzan, and J. E. Subotnik, Energy-Efficient Pathway for Selectively Exciting Solute Molecules to High Vibrational States via Solvent Vibration-Polariton Pumping, *Nature Communications* **13**, 4203 (2022).
- [161] T. E. Li and S. Hammes-Schiffer, QM/MM Modeling of Vibrational Polariton Induced Energy Transfer and Chemical Dynamics, *Journal of American Chemical Society* **145**, 377 (2023).
- [162] D. P. Kovács, J. H. Moore, N. J. Browning, I. Batatia, J. T. Horton, V. Kapil, W. C. Witt, I.-B. Magdău, D. J. Cole, and G. Csányi, *MACE-OFF23: Transferable Machine Learning Force Fields for Organic Molecules* (2023), arXiv:2312.15211.
- [163] M. Parrinello and A. Rahman, Study of an F center in molten KCl, *The Journal of Chemical Physics* **80**, 860 (1984).
- [164] T. J. H. Hele, M. J. Willatt, A. Muolo, and S. C. Althorpe, Boltzmann-conserving classical dynamics in quantum time-correlation functions: “Matsubara dynamics”, *The Journal of Chemical Physics* **142**, 134103 (2015).
- [165] S. C. Althorpe, Path-integral approximations to quantum dynamics, *The European Physical Journal B* **94**, 155 (2021).
- [166] M. Rossi, M. Ceriotti, and D. E. Manolopoulos, How to remove the spurious resonances from ring polymer molecular dynamics, *The Journal of Chemical Physics* **140**, 234116 (2014).
- [167] M. J. Willatt, M. Ceriotti, and S. C. Althorpe, Approximating Matsubara dynamics using the planetary model: Tests on liquid water and ice, *The Journal of Chemical Physics* **148**, 102336 (2018).
- [168] G. Trenins, M. J. Willatt, and S. C. Althorpe, Path-integral dynamics of water using curvilinear centroids, *The Journal of Chemical Physics* **151**, 054109 (2019).
- [169] C. Haggard, V. G. Sadhasivam, G. Trenins, and S. C. Althorpe, Testing the quas centroid molecular dynamics method on gas-phase ammonia, *The Journal of Chemical Physics* **155**, 174120 (2021).
- [170] A. Witt, S. D. Ivanov, M. Shiga, H. Forbert, and D. Marx, On the applicability of centroid and ring polymer path integral molecular dynamics for vibrational spectroscopy., *The Journal of Chemical Physics* **130**, 194510 (2009).
- [171] V. Kapil, D. P. Kovács, G. Csányi, and A. Michaelides, First-principles spectroscopy of aqueous interfaces using machine-learned electronic and quantum nuclear effects, *Faraday Discuss.* **249**, 50 (2024).
- [172] A. Singraber, J. Behler, and C. Dellago, Library-Based LAMMPS Implementation of High-Dimensional Neural Network Potentials, *Journal of Chemical Theory and Computation* **15**, 1827 (2019).
- [173] S. Batzner, A. Musaelian, L. Sun, M. Geiger, J. P. Mailoa, M. Kornbluth, N. Molinari, T. E. Smidt, and B. Kozinsky, E(3)-equivariant graph neural networks for data-efficient and accurate interatomic potentials, *Nature Communications* **13**, 2453 (2022).
- [174] I. Batatia, D. P. Kovacs, G. Simm, C. Ortner, and G. Csanyi, MACE: Higher Order Equivariant Message Passing Neural Networks for Fast and Accurate Force Fields, *Advances in Neural Information Processing Systems* **35**, 11423 (2022).
- [175] S. Mukamel, *Principles of Nonlinear Optical Spectroscopy* (Oxford University Press, 1999).
- [176] M. Grechko, T. Hasegawa, F. D’Angelo, H. Ito, D. Turchinovich, Y. Nagata, and M. Bonn, Coupling between intra- and intermolecular motions in liquid water revealed by two-dimensional terahertz-infrared-visible spectroscopy, *Nature Communications* **9**, 885 (2018).
- [177] P. Seliya, M. Bonn, and M. Grechko, On selection rules in two-dimensional terahertz–infrared–visible spectroscopy, *The Journal of Chemical Physics* **160**, 034201 (2024).
- [178] K. A. Jung, P. E. Videla, and V. S. Batista, Ring-polymer, centroid, and mean-field approximations to multi-time Matsubara dynamics, *The Journal of Chemical Physics* **153**, 124112 (2020).
- [179] K. A. Jung, P. E. Videla, and V. S. Batista, Inclusion of nuclear quantum effects for simulations of nonlinear spectroscopy, *The Journal of Chemical Physics* **148**, 244105 (2018).
- [180] Z. Tong, P. E. Videla, K. A. Jung, V. S. Batista, and X. Sun, Two-dimensional Raman spectroscopy of Lennard-Jones liquids via ring-polymer molecular dynamics, *The Journal of Chemical Physics* **153**, 034117 (2020).
- [181] F. Aryasetiawan and F. Nilsson, *Downfolding Methods in Many-Electron Theory* (AIP Publishing LLC, 2022) <https://pubs.aip.org/book-pdf/12252618/9780735422490.pdf>.
- [182] J. Berges, N. Girotto, T. Wehling, N. Marzari, and S. Poncé, Phonon self-energy corrections: To screen, or not to screen, *Physical Review X* **13**, 041009 (2023).
- [183] X.-M. Zhao, K. Zhang, Z.-Y. Cao, Z.-W. Zhao, V. V. Struzhkin, A. F. Goncharov, H.-K. Wang, A. G. Gavriliuk, H.-K. Mao, and X.-J. Chen, Pressure tuning of the

charge density wave and superconductivity in $2h - \text{TaS}_2$,
[Physical Review B **101**, 134506 \(2020\)](#).